JGR Solid Earth

RESEARCH ARTICLE
10.1029/2023JB026418

Remagnetization Under Hydrothermal Alteration of South Tibetan Paleocene Lavas: Maghemitization, Hematization, and Grain Size Reduction of (Titano)magnetite

Wentao Huang[1], Shanshan Niu[2], Mark J. Dekkers[3], Peter C. Lippert[4], Dario Bilardello[5], Peat Solheid[5], Bo Zhang[6], Guillaume Dupont-Nivet[7], Douwe J. J. van Hinsbergen[3], and Lin Ding[1]

[1]State Key Laboratory of Tibetan Plateau Earth System, Environment and Resources (TPESER), Institute of Tibetan Plateau Research, Chinese Academy of Sciences, Beijing, China, [2]North China Electric Power University, Beijing, China, [3]Department of Earth Sciences, Utrecht University, Utrecht, The Netherlands, [4]Department of Geology and Geophysics, University of Utah, Salt Lake City, UT, USA, [5]Institute for Rock Magnetism, Department of Earth Sciences, University of Minnesota, Minneapolis, MN, USA, [6]Key Laboratory of Orogenic Belts and Crustal Evolution, Ministry of Education, School of Earth and Space Sciences, Peking University, Beijing, China, [7]Géosciences Rennes, UMR 6118, Université de Rennes 1, Rennes, France

Abstract The Paleocene lavas from Dianzhong Formation (E_1d) in Linzhou basin of southern Lhasa terrane are a key target for paleomagnetic investigations into the timing and paleolatitude of the initial India-Asia collision. Controversy exists, however, on whether these rocks preserve a primary remanent magnetization. Here we reanalyze previously published thermal demagnetization data and report detailed rock magnetic results and petrographic observations of these rocks. We find that the original magnetic carrier, a magmatic multidomain Ti-poor titanomagnetite, underwent significant grain size reduction and was variably reacted to single-domain maghemite and nano-hematite. Such strong alteration may have resulted from successive hydrothermal events: a first event related to the ~52 Ma dike intrusions into the E_1d that accompanied a massive ignimbrite eruption deposited above the E_1d producing heating up to 300°C; and a secondary event related to the 42–27 Ma southward overthrusting of the basin, heating the E_1d up to 130–145°C. Unblocking/inversion temperature spectra of the authigenic maghemite and nano-hematite overlap with those of the titanomagnetite, implying that the primary remanence of the E_1d lavas has been contaminated or replaced by thermoviscous and chemical remanent magnetizations. Thus the isolated characteristic remanent magnetization from these rocks, whether slightly or completely altered, cannot be considered primary and should not be used for paleolatitudinal determination. Our study confirms that hydrothermal alteration can seriously jeopardize the remanence carried by titanomagnetite and thus should be tested for paleomagnetic investigations of rock units from tectonically active areas.

Plain Language Summary The study of past magnetic directions preserved in rocks (paleomagnetism) enables to constrain the paleolatitudes of the southern Asian margin where the rocks formed and is thus key to understand the timing and latitude of the initial India-Asia collision. However, paleomagnetic studies of Paleogene rocks of southern Tibet have returned a surprisingly wide spread of paleolatitude data. One possible explanation is unrecognized remagnetization, a process that may relate to subsequent hydrothermal alteration. Such hydrothermal alteration has recently been documented for Paleocene lavas in the Linzhou basin, paleomagnetic signals from which have previously been interpreted either as primary or secondary (re) magnetizations. Here we analyze previously published and newly acquired paleomagnetic, rock magnetic, and petrographic data of these rocks to identify whether hydrothermal alteration caused remagnetization, and how such events may be fingerprinted. We find that the original magnetic carrier is Ti-poor titanomagnetite. Hydrothermal alteration, however, led to significant changes in these titanomagnetite crystals and mineral transformations to maghemite and hematite, associated with acquisition of secondary magnetizations with the magnetic behaviors similar to the primary magnetization. This can be misleading for the interpretation of the magnetic directions obtained from these rocks and imply that they are not suitable for paleolatitudinal determination.

Key Points:

- Hydrothermal alteration intensively destroyed the original multi-domain titanomagnetite and recorded magnetization in the Dianzhong lavas
- Titanomagnetite experienced serious grain size reduction and has variably converted to authigenic single-domain maghemite and nano-hematite
- Primary remanent magnetization has been replaced or contaminated, these lavas should not be used to determine Lhasa terrane paleolatitude

Supporting Information:

Supporting Information may be found in the online version of this article.

Correspondence to:

W. Huang,
whuang@itpcas.ac.cn

Citation:

Huang, W., Niu, S., Dekkers, M. J., Lippert, P. C., Bilardello, D., Solheid, P., et al. (2023). Remagnetization under hydrothermal alteration of south Tibetan Paleocene lavas: Maghemitization, hematization, and grain size reduction of (Titano)magnetite. *Journal of Geophysical Research: Solid Earth*, *128*, e2023JB026418. https://doi.org/10.1029/2023JB026418

Received 14 JAN 2023
Accepted 5 MAR 2023

Author Contributions:

Conceptualization: Wentao Huang
Formal analysis: Wentao Huang, Shanshan Niu
Funding acquisition: Wentao Huang, Lin Ding
Investigation: Wentao Huang, Shanshan Niu
Methodology: Mark J. Dekkers, Dario Bilardello, Peat Solheid, Bo Zhang
Project Administration: Wentao Huang
Resources: Lin Ding
Software: Dario Bilardello, Peat Solheid
Writing – original draft: Wentao Huang

Writing – review & editing: Mark J. Dekkers, Peter C. Lippert, Dario Bilardello, Peat Solheid, Guillaume Dupont-Nivet, Douwe J. J. van Hinsbergen, Lin Ding

1. Introduction

Magnetite (Fe_3O_4), a mixed-valence iron oxide with an inverse cubic spinel structure at room temperature (Verwey, 1939), is one of the most common ferromagnetic minerals targeted in paleomagnetic studies. However, the metastability of ferrous iron (Fe^{2+}) within the magnetite lattice leads to its transformation under high oxygen fugacity conditions to maghemite (γ-Fe_2O_3) and/or hematite (α-Fe_2O_3), which contain only ferric iron (Fe^{3+}). Maghemite has the same inverse cubic spinel structure as magnetite but has a smaller unit cell (Dunlop & Ödemir, 1997), its inversion from magnetite requires weakly acidic conditions and/or low temperature, because the lattice is not destroyed. In contrast, hematite has a hexagonal crystal structure and its formation from magnetite requires strongly acidic conditions, oxidizing agents, and/or high temperature with lattice destruction involved. Transformation of magnetite to maghemite and hematite is ubiquitous in nature, which, if postdating the recording of the primary remanent magnetization, complicates the interpretation of the natural remanent magnetization (NRM), jeopardizing the determination of the primary direction and paleointensity (e.g., Almeida et al., 2014; Bleil & Petersen, 1983; Cui et al., 1994; Elmore et al., 2012; Gribov et al., 2017; Thomas, 1993; Xu et al., 1997). Chemical remanent magnetization (CRM) carried by authigenic hematite precipitated during later hydrothermal alteration of magnetite has been well described on several occasions in igneous rocks (e.g., Edel & Aifa, 2001; Geissman & Harlan, 2002; Huang, Dupont-Nivet, et al., 2015; Swanson-Hysell et al., 2019). Likewise, paleomagnetic investigation of maghemite often focuses on its formation conditions, magnetic properties, relation to self-reversed magnetization in rocks, and effects on geomagnetic paleointensity determination (e.g., Almeida et al., 2015; Cui et al., 1994; Doubrovine & Tarduno, 2004; Fabian, 2009; Ge et al., 2014; Krása et al., 2005; Liu et al., 2004; Swanson-Hysell et al., 2011; Özdemir & Dunlop, 2010). Although experimental conversion of magnetite to maghemite and hematite under hydrothermal conditions has been studied in the laboratory (e.g., Jolivet & Tronc, 1988; Otake et al., 2007), such a transformation and its effects on the preservation of the primary remanence have been rarely documented in natural rocks subjected to high-temperature hydrothermal alteration.

Here we study a set of Paleocene lavas from the lower Linzizong Group, exposed in the Linzhou basin of the southern Lhasa terrane, which have been the primary target for determining the Paleogene latitude of the Lhasa terrane, dating the India-Asia collision, and constraining the post-collisional shortening of Asia. Previous paleomagnetic studies have argued that these lavas retain a primary remanence, determining a paleolatitude of ~6°N for the Lhasa terrane in the early Paleocene (Chen et al., 2010, 2014; Yi et al., 2021). Such latitude is much lower than the determined Cretaceous and early Eocene latitudes of ~20°N (e.g., Bian et al., 2020; Huang et al., 2013; Huang, Dupont-Nivet, et al., 2015; Lippert et al., 2014; Ma et al., 2017). Such discrepancy in paleolatitudes would imply rapid "yo-yo-like" plate tectonic motions of the Lhasa terrane (Yi et al., 2021), requiring rapid opening and closing of back-arc basins, a scenario for which there is little independent evidence. Our previous investigations of these rocks reveal that they were possibly hydrothermally remagnetized due to acquisition of a CRM residing in authigenic hematite and a thermoviscous remanent magnetization (TVRM) carried by magmatic (titano)magnetite following hydrothermal events (Huang et al., 2015a, 2023). These hypotheses left unanswered questions as to why slightly altered lavas with little hematite concentration record a similar remanence direction to that of highly altered lavas with significant amounts of hematite, and why the high-temperature component (HTC, isolated at 580–680°C) carried by hematite is indistinguishable in direction from the intermediate temperature component (ITC, isolated at 350–580°C) carried by Ti-poor titanomagnetite. Here, we reanalyze the thermal demagnetization behaviors of these rocks, conduct comprehensive rock magnetic and Mössbauer spectroscopic experiments, and apply scanning electron microscopy (SEM) observation with associated energy-dispersive X-ray spectrometry (EDS) analysis. We use these results to determine the magnetic carriers of these rocks, their grain sizes, and interpret their formation processes. We then discuss the remanence destruction/acquisition following the alteration/formation of these magnetic minerals during hydrothermal alteration, and the origin of the NRMs in these rocks. Finally, we discuss the potential mechanisms of modification of the primary remanences residing in titanomagnetite by subsequent hydrothermal alteration events in an attempt of bridging the gap between rock magnetism and paleomagnetic investigations in the context of the India-Asia collision.

2. Geologic and Paleomagnetic Background

The southern margin of the Lhasa terrane exposes the E-W trending Gangdese magmatic belt (Figures 1a and 1b) comprising the long-lived volcanic arc that formed during the northward subduction of the Neotethyan oceanic lithosphere beneath Eurasia. The belt is composed of the Gangdese batholith and associated Linzizong Group

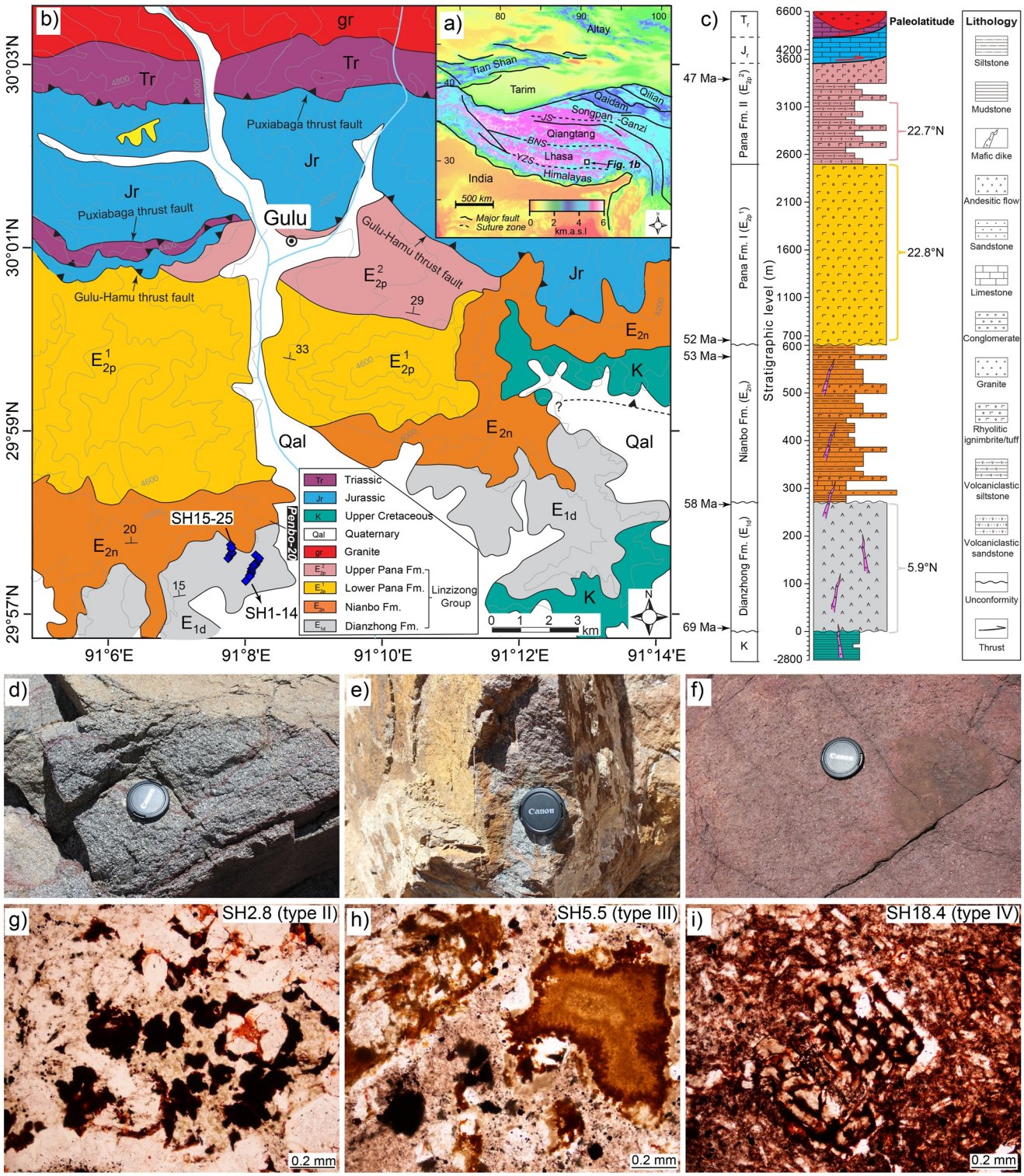

Figure 1.

volcanic rocks (e.g., Ding et al., 2003; Yin & Harrison, 2000). Eruption of the Linzizong Group has been dated to ~69–41 Ma, during which time the first accretion of continent-derived crustal units that now comprises the northern units of the Himalayan fold-thrust belt occurred (e.g., An et al., 2021; Cai et al., 2011; DeCelles et al., 2014; Ding et al., 2016; Hu et al., 2015; Hu et al., 2016). This temporal overlap of collision and accretion has made the

Linzizong Group a prime target for investigating the paleolatitude history of the Lhasa terrane to determine how the post-collisional convergence was distributed within the orogenic system (e.g., Dupont-Nivet et al., 2010).

Geochronology, low-temperature thermochronology, paleoaltimetry and paleomagnetic studies of the Linzizong Group have mostly focused on the volcanic-sedimentary successions exposed in the Linzhou basin (e.g., Achache et al., 1984; BGMRXAR, 1993; Chen et al., 2010; Chen et al., 2016; Ding et al., 2014; Dupont-Nivet et al., 2010; He et al., 2007; Huang et al., 2022; Ingalls et al., 2018; Liu, 1993; Mo et al., 2003; Tan et al., 2010). Here, the Linzizong Group has a total thickness of 3.5 km and is divided into the Dianzhong (E_1d, 69–58 Ma, zircon U-Pb ages, same for below), Nianbo (E_2n, 58–53 Ma), and Pana (E_2p, 53–47 Ma) formations upsection (Figure 1c). The E_1d strata (270 m thick) are mainly composed of andesitic lavas (Figure 1d). The E_2n strata (330 m thick) contain two repeated sequences of mudstone, conglomerate, limestone, and tuff layers. The E_2p consists of massive ignimbrite in the lower part (E_2p^1, 1,800 m thick) and interbedded sandstone, mudstone, and tuff deposits in the upper part (E_2p^2, 1,100 km thick). The E_1d, E_2n, as well as underlying deformed Cretaceous redbeds were pervasively intruded by mafic dykes at ~52 Ma (He et al., 2007; Yue & Ding, 2006). Lavas of the E_1d, which are the target of this research, have been variably hydrothermally altered (Huang et al., 2022). The color of the rocks changes from gray to yellowish and reddish with increasing alteration (Figures 1e–1g). These color changes were used in conjunction with thermal demagnetization behaviors and petrographic observations to subdivide the studied samples into four groups (types I–IV, more in Section 3 below). Strongly altered reddish lavas are commonly observed below the unconformity between the E_1d and E_2n (Figure 1d) and near the dykes (Huang, Dupont-Nivet, et al., 2015).

Ignimbrites and volcanoclastic sandstones from the E_2p are generally fresh, and they have straightforward demagnetization trajectories with the characteristic remanent magnetization (ChRM) isolated by both thermal and alternating field (AF) demagnetization treatments. The E_2p^1 and E_2p^2 rocks have yielded a consistent mean inclination of ~40°, corresponding to a paleolatitude of ~23°N after averaging paleosecular variation in the E_2p^1 volcanic rocks and correcting for inclination shallowing in the E_2p^2 sedimentary rocks (Figure 1c) (Dupont-Nivet et al., 2010; Huang et al., 2013). In contrast, E_1d lavas have complex demagnetization behaviors. Sample types I–III (descriptions of the types I–IV samples are provided in the first paragraph in Section 3) from the E_1d lavas record an overprint of normal polarity which can be revealed by AF or thermal demagnetization (Figures 2a–2j). This overprint, isolated below 300°C, has been defined as a low-temperature component (LTC) with a mean direction of $D_g/I_g = 0.8°/41.1°$ and $D_s/I_s = 359.0°/26.7°$ (D: declination, I: inclination, g: geographic coordinates, s: stratigraphic coordinates) (Huang, Dupont-Nivet, et al., 2015). After removing the LTC, an ITC between 350°C and 580°C is isolated from all the samples; this ITC is of reversed polarity for most samples (Figures 2a–2h, 2j-2l), but in some type III samples yield an ITC of normal polarity was identified (Figure 2i). A HTC is isolated from types II–IV samples from 580 to 680°C, and is usually of reversed polarity (Figures 2e–2h, 2j–2l), except for some type III samples (Figure 2i). The directions of the ITC and HTC are generally indistinguishable in the same sample, except for a few type III samples (Figure 2h). The intensity of the NRM for types I–II samples is 1–2 orders of magnitude stronger than that of types III–IV samples (Figure 2). The NRM decay curves (vector difference sum) vary from sample to sample, indicating that the magnetic carriers of each component, and their domain states, are complex. For types I–II samples recording a strong LTC, there is a remarkable decrease of the NRM before 300°C, which is also clearly shown by the corresponding unblocking spectra (Figures 2a–2g). The unblocking spectra for the ITC in types I–III samples vary a lot in temperature and can generally be divided into two ranges of 350–540°C and 540–580°C (Figure 2). The unblocking spectra for the HTC in types II–IV samples cover the whole temperature range of 580–680°C (Figure 2). The ITC and/or HTC have been interpreted as the characteristic remanent magnetization (ChRM) of the E_1d lavas, and together they define a mean ChRM direction of $D_g/I_g = 195.9°/-25.4°$ and $D_s/I_s = 193.5°/-11.6°$, corresponding to paleolatitude of ~6°N (Huang, Dupont-Nivet, et al., 2015), ~17° lower than the paleolatitude of ~23°N determined from the robust paleomagnetic results of the E_2p volcanic and sedimentary rocks (Figure 1c).

Figure 1. (a) Location of the study area on a digital elevation model of the India-Asia collision zone, modified from Dupont-Nivet et al. (2010). YZS, Yarlung Zangbo suture; BNS, Bangong-Nujiang suture; JS, Jinsha suture; (b) geologic map of the Linzhou basin and paleomagnetic sampling localities (blue diamonds) of the Dianzhong lavas reported in Huang, Dupont-Nivet, et al. (2015) and reanalyzed in this study; (c) stratigraphic column of the Linzhou basin and summary of geochronologic and paleomagnetic results, modified from Huang et al. (2022). The paleolatitudes from the Dianzhong lavas, lower Pana ignimbrites and upper Pana volcaniclastic sandstones (after correction of inclination shallowing) are reported in Huang, Dupont-Nivet, et al. (2015), Dupont-Nivet et al. (2010), and (Huang et al., 2013), respectively. (d)–(f) Field observations of lavas from the Dianzhong Formation (E_1d) of the Linzizong group with increasing alteration. (g)–(i) Petrographic observations of thin sections from the andesitic E_1d lavas under plane polarized light show that alteration of feldspar and biotite to sericite, calcite and rutile is widespread, and is characterized by precipitation of secondary hematite along cracks, within voids and surrounding Fe-bearing silicates. SH2.8 (g) is moderately altered, SH5.5 (h) is strongly altered and SH18.4 (i) is completely altered.

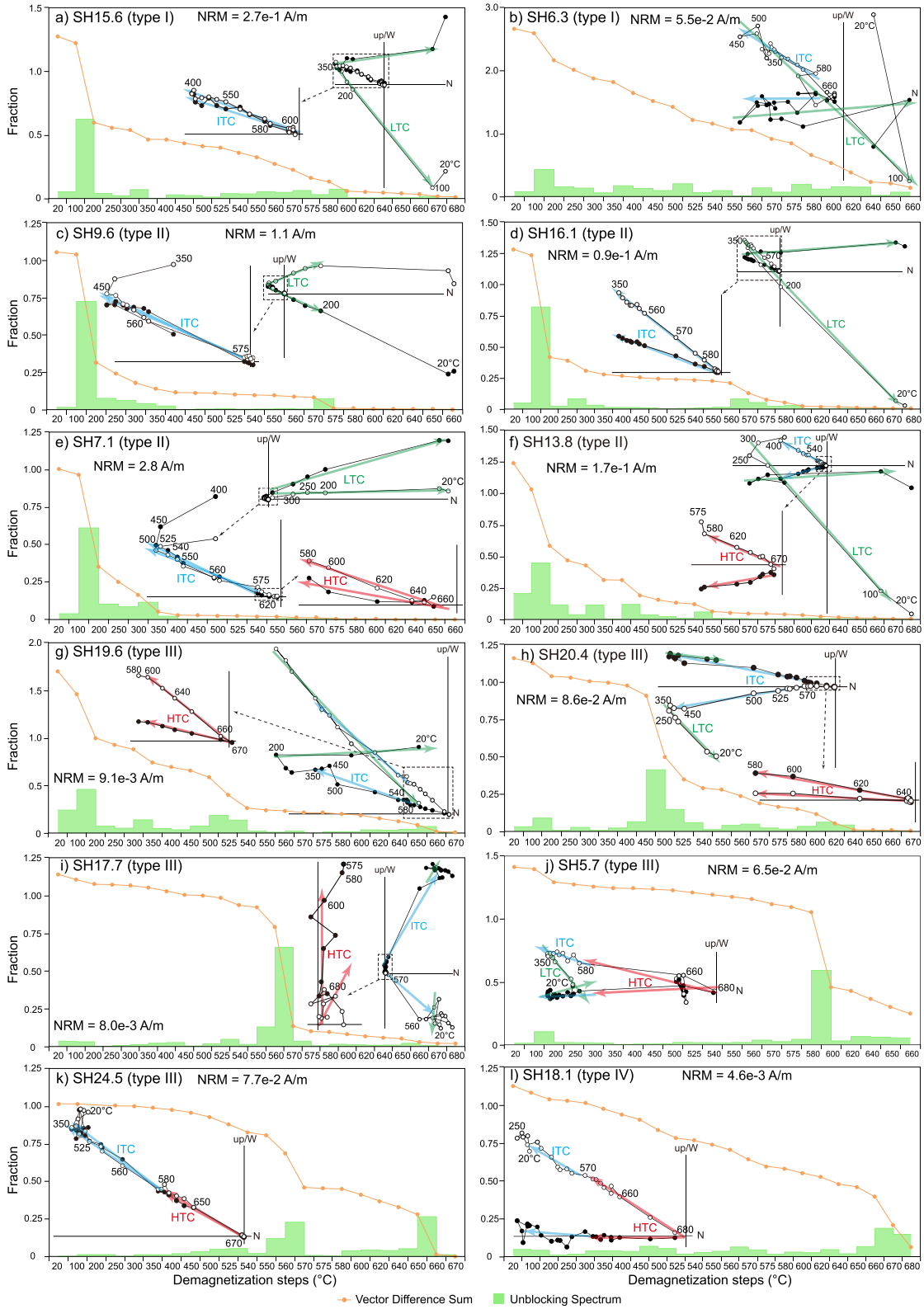

Figure 2. Thermal demagnetization trajectories and corresponding decay of the NRM of representative samples from the E_1d lavas, analyzed with the online program www.paleomagnetism.org (Koymans et al., 2016, 2020). All demagnetization diagrams are displayed in geographic coordinates. Closed (open) symbols represent the projection of vector endpoints on the horizontal (vertical) plane; values represent thermal demagnetization steps in °C. LTC: low-temperature component, ITC: intermediate-temperature component, HTC: high-temperature component.

3. Results

Based on visual description and petrographic observations (Figure 1) and distinct thermal demagnetization behaviors (see Section 2 above), we divide samples from the E_1d lavas into four types. Type I samples are dark gray and slightly altered, type II samples are light gray and moderately altered, type III samples are brown to yellowish and strongly altered, and type IV samples are reddish and (nearly) completely altered. We selected a series of slightly to completely altered samples from each type and applied combined rock magnetic, Mössbauer spectroscopic and microscopic analyses to investigate the magnetic carriers and their domain states, morphology, and formation. Measurement procedures and data analysis protocols are presented in Supporting Information S1.

3.1. High-Temperature Dependence of Magnetic Susceptibility

Repeated magnetic susceptibility versus temperature (χ-T) curves of the type I sample (Figure 3a) show a steady increase in susceptibility upon heating to 300°C; this susceptibility increase is nearly reversible upon cooling to room temperature. A gradual decrease of the susceptibility is observed when heating further between 300 and 500°C, and the lost susceptibility is not recovered on cooling, suggesting the inversion of maghemite to hematite (e.g., Bilardello, 2020; Gehring et al., 2009; Kontny & Grothaus, 2017). The heating curve up to 600°C is characterized by a sharp decrease in susceptibility between 530°C and 580°C. This defines an estimated Curie temperature of 549°C, indicative of Ti-poor titanomagnetite ($x = 0.06$) as the dominant magnetic carrier (Dunlop & Ödemir, 1997; Lattard et al., 2006). The heating curve up to 700°C mimics the previous heating curve with little susceptibility remaining above 600°C, and the subsequent cooling curve being irreversible and much lower in susceptibility.

The heating curves of type II samples (Figures 3b and 3c) show a large increase in susceptibility up to 300°C with a very rapid raise at 100–150°C. The following cooling curves are irreversible. The heating curves up to 500°C are characterized by a gradual increase in susceptibility before ~300°C, followed by a rapid decrease in susceptibility afterward. Such quick increase and decrease in susceptibility form a "maghemite bump" with two shoulders between 150°C and 260–320°C. The increase in susceptibility is likely not induced by formation of new magnetic minerals, but is instead attributed to the annealing of stresses in the maghemite lattice (e.g., Appel, 1987; Zhang et al., 2021), whereas the decrease corresponds to the inversion of maghemite to hematite (Bilardello, 2020; Kontny & Grothaus, 2017). The following heating and cooling curves up to 600°C and 700°C are irreversible, they show a quick decrease in susceptibility between 530 and 560°C and 600°C, followed by a continual loss of susceptibility until 620–650°C. The first derivative of the susceptibility versus temperature in the heating curves defines an estimated Curie temperature of 560°C for sample SH1.6, corresponding to the unblocking of Ti-poor titanomagnetite with x = 0.03 (a general formula for titanomagnetite of $Fe_{3-x}Ti_xO_4$) (Butler, 1992). Another defined temperature transition at 591°C for sample SH13.8 and 604°C for sample SH1.6 may indicate the unblocking of some maghemite that has survived the inversion to hematite, or it may be newly created hematite. We realize, however, that it is difficult to determine the Curie temperature of maghemite accurately because it inverts to hematite during heating. Maghemite has a variable Curie temperature of 420–645°C (De Boer et al., 2001; Dunlop & Ödemir, 1997), depending on the method of sample preparation, grain size and shape, impurities, reaction pressure and atmosphere, and annealing time (Gendler et al., 2005). Comparison of the room temperature susceptibility of the sample before and after the heating/cooling cycles reveals that ~80–90% of susceptibility was lost during the procedure.

The χ-T curves of type III samples vary from sample to sample. Heating and cooling curves of sample SH19.6 (Figure 3d) are similar to these of type II samples. The estimated Curie temperature of 556°C and 598°C corresponds to those of Ti-poor titanomagnetite and maghemite, respectively, or unblocking of newly created hematite for the latter. Sample SH5.7 (Figure 3e) shows a gradual increase in susceptibility upon heating to 300°C. The decrease in susceptibility is clear between 300°C and 500°C, and a maghemite bump is also recognized in this sample. The heating and cooling curves up to 600°C are characterized by a rapid decrease in susceptibility at 500–600°C upon heating, followed by a rapid increase in susceptibility (up to 100 times higher) upon cooling. The rapid decrease in the heating curve defines an estimated Curie temperature of 568°C, indicative of Ti-poor titanomagnetite. It is likely that this sample contains more iron-bearing clay minerals or phyllosilicates, leading to their alteration to magnetite during heating as shown by the irreversibility of the cooling curves. The heating curve to 700°C show a continual decrease of the susceptibility up to the maximum heating temperature. For sample SH17.7 (Figure 3f), the heating and cooling curves up to 300°C are stable and reversible. The heating

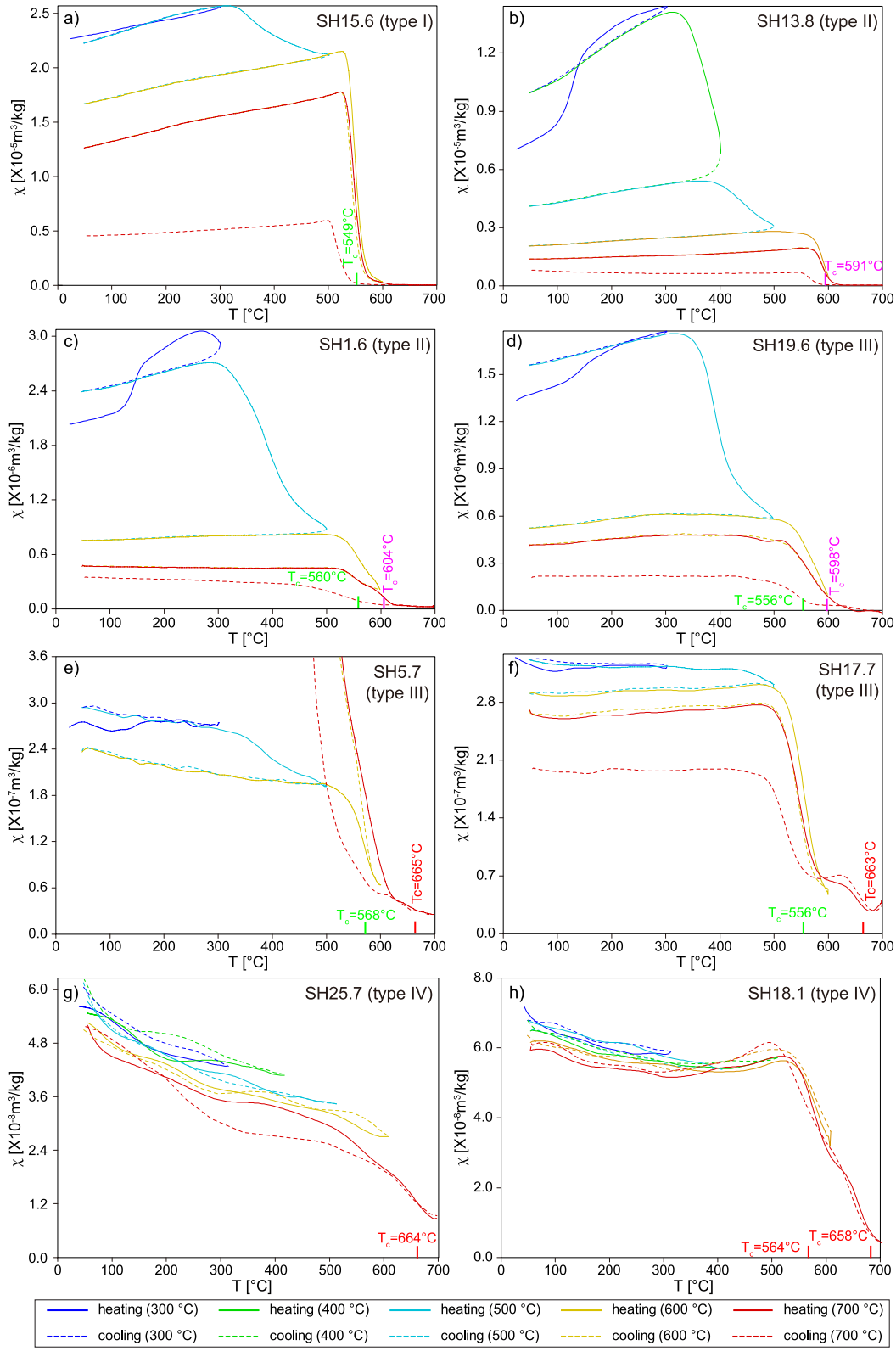

Figure 3. Multicycle high-temperature bulk magnetic susceptibility versus temperature (χ-T) measurements in air for representative types I–IV samples. The Curie temperatures for titanomagnetite (green), maghemite (purple), and hematite (red) that are estimated from sharp decrease of the susceptibility upon heating are also marked.

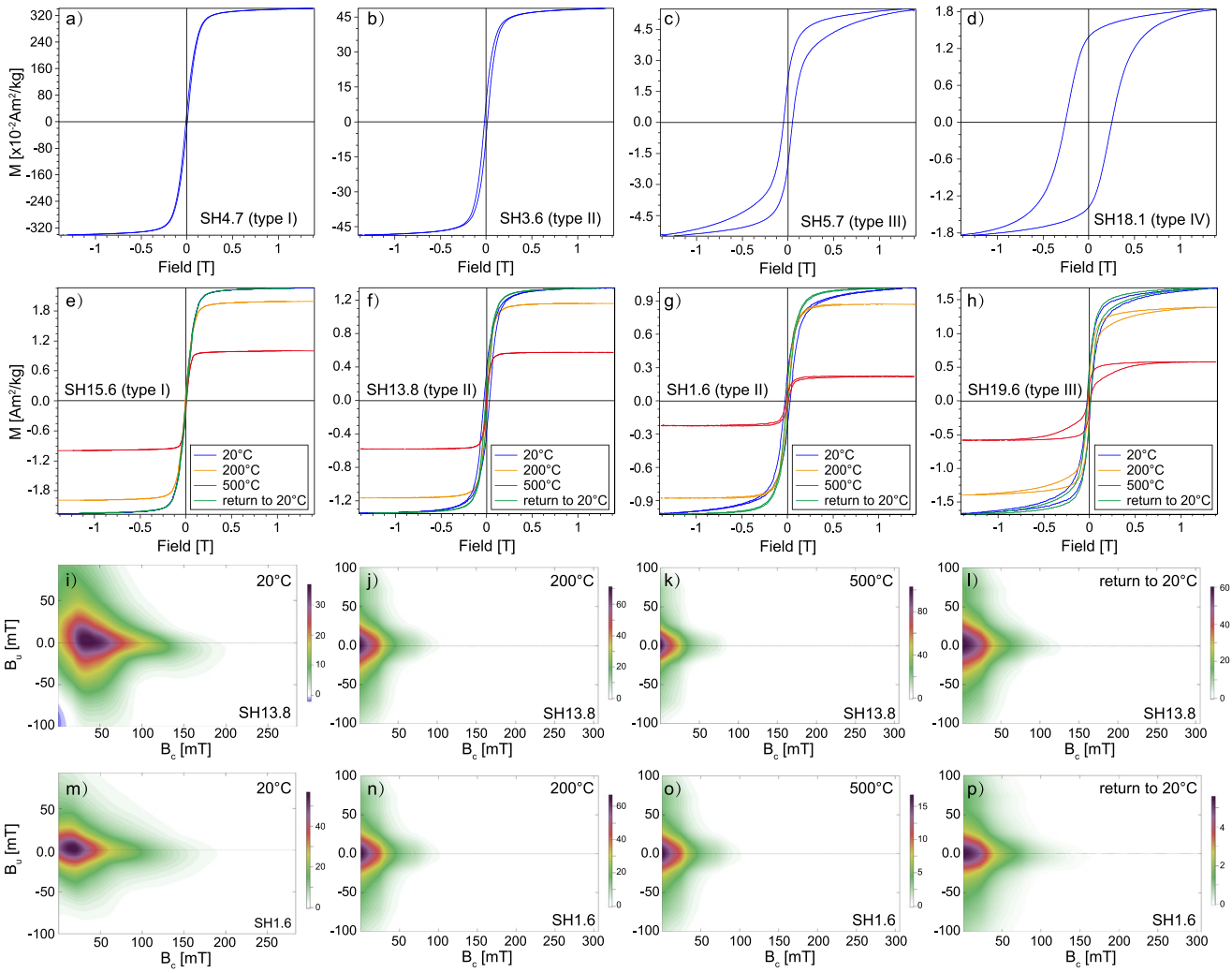

Figure 4. (a–d) Room-temperature hysteresis loops of representative types I–IV samples. (e–h) Room-temperature (20°C, before and after heating) and high-temperature (200°C, 500°C) hysteresis loops of representative types I–IV samples. (i–l) Corresponding FORC diagrams of a type II sample SH13.8 at room-temperature (20°C, before and after heating) and high-temperature (200°C, 500°C). (m–p) Similar FORC diagrams of another type II sample SH1.6.

and cooling curves up to 500°C show gentle loss of susceptibility and are irreversible. A distinct decrease in susceptibility between 500°C and 600°C defines an estimated Curie temperature of 556°C, representing Ti-poor titanomagnetite. Further decrease in susceptibility upon heating to 700°C determines a disordering temperature of 663°C, which is close to the typical Néel temperature of hematite of 675°C.

The χ-T curves of type IV samples are general reversible for all cycles (Figures 3g and 3h). Sample SH25.7 features a linear decrease in susceptibility up to 600°C and an accelerated decrease between 600 and 700°C. Such a wide unblocking temperature range indicates that the dominant magnetic carrier is fine-grained hematite. Sample SH18.1 shows a decrease in susceptibility up to 300°C and a gradual increase in susceptibility up to 520°C, followed by a sharp decrease in susceptibility between 520 and 700°C. The estimated Curie temperatures are 564 and 658°C, both representing hematite in different grain sizes (Swanson-Hysell et al., 2019), as confirmed by the following rock magnetic analysis.

3.2. Room-Temperature and High-Temperature Hysteresis Measurements

The room-temperature hysteresis loops of type I samples are narrow and are saturated below 1 T (Figures 4a and 4e, panels e–h contain hysteresis loops measured at room-temperature of 20°C). Bulk coercivity (B_c) values are <10 mT and remanent coercivity (B_{cr}) values are <45 mT (Table S1 in Supporting Information S1). Hysteresis

loops of the type II samples are slightly open (Figures 4b, 4f and 4g), their B_c values range 1–40 mT and the B_{cr} values determined from backfield demagnetization curves range 46–125 mT (Table S1 in Supporting Information S1). Type III samples are characterized by wasp-waisted hysteresis loops (Figures 4c and 4h), indicative of the presence of magnetic minerals with contrasting coercivities or grain sizes (Tauxe et al., 1996). These samples have notably variable B_c and B_{cr} values of 21–81 mT and 76–420 mT (Table S1 in Supporting Information S1), respectively. Type IV samples have rectangular hysteresis loops (Figure 4c) and very high B_c and B_{cr} values (>200 mT, Table S1 in Supporting Information S1), which is typical of hematite.

We use five statistically significant components to fit the coercivity spectra in the component analysis of the isothermal remanent magnetization (IRM) acquisition curves of the E_1d samples using MAX UnMix (Maxbauer et al., 2016) (Figure 5; Table S3 in Supporting Information S1). Component 1 appears only in type I samples; it has very low B_h values (mean coercivity of an individual grain population) values of 19–23 mT. Component 2 is required to fit the coercivity spectra of types I–III samples: its B_h values vary from 30 to 62 mT with the most values < 45 mT. Component 3 appears in all sample types; it has relatively high B_h values of 73–142 mT. Components 4 and 5 have the highest B_h values of 247–453 mT and 564–1109 mT, respectively, and are required to fit the coercivity spectra of types II–IV samples. Together with the results from the χ-T curves and hysteresis loops, we interpret components 1 and 2 to be titanomagnetite with different grain size populations, component 3 to be maghemite for all the samples except SH17.7, where it represents titanomagnetite with smaller grain size (indicated by the low-temperature measurements described in Section 3.3), and components 4 and 5 to be hematite with different grain sizes. The contribution of titanomagnetite to the IRM is 78%–93% for type I samples, 16%–54% for type II samples, 0%–44% for type III samples, and 0% for type IV samples. Maghemite constitutes 7%–22% of the IRM in type I samples, 46%–84% in type II samples, 26%–81% in type III samples, and 7%–16% in type IV samples. Hematite has no to little (0%–5%) contribution to the IRM of type I and II samples, whereas its contributions to the IRM of types III and IV samples are variable (19%–65%) and very high (84%–93%), respectively. For the types I and II samples, the contribution of maghemite to the IRM increases with a concomitant decrease of the titanomagnetite contribution to the IRM (Figure 6a). In the Day plot (M_s: saturation magnetization, M_{rs}: remanent saturation) (Dunlop, 2002), types I and II samples distribute along the single-domain (SD) and multidomain (MD) (titano)magnetite mixing curves (Figure 6b). The domain states of the bulk magnetic carriers also vary systematically from MD to pseudo-single domain (PSD)-SD with increasing amount of maghemite and decreasing amount of titanomagnetite, implying that maghemite is possibly in SD state and titanomagnetite is close to the MD states in the types I and II samples. Although interpretation of magnetic grain size from Day plots in mixed composition rocks can be non-unique (e.g., Roberts et al., 2018), our interpretations are further confirmed by the first-order reversal curve (FORC) diagrams of the same samples. In FORC diagrams, type I samples show major FORC density along the B_u axis, indicative of MD state grains. Less pronounced FORC density appears along the B_c axis up to ~150 mT indicative of a population of smaller grains with higher coercivities. In contrast, type II samples show more triangular distributions centered around higher coercivities, with negative indentations oriented 135° (most clear in panel 5e but evident as well from the shape of the lower lobes in panels 5d, 5f, and 5g) diagnostic of vortex state (PSD-behavior) grains, and more prominent high coercivity distributions that extend to >200 mT indicative of harder SD grains (Figure 5). We note that presence of uniaxial hematite may contribute to the high coercivity distributions along the B_c axes (Roberts et al., 2021). Types I and II samples also show a nearly linear trend between M_{rs}/M_s and B_c values on a Néel, or squareness plot (Tauxe et al., 2002), indicating a trend of grain size reduction from types I to type II samples (Figure 6c). The least-square regression line through these data does not go through the origin of the plot and deviates from the line for unoxidized stoichiometric magnetite. We attribute this to the combined effects of the decrease of M_s and the independent increase of B_c with increasing oxidation (Wang & Van der Voo, 2004). For type III samples with large amounts of hematite, the pattern of the FORC diagrams also depends on the relative concentration of maghemite to titanomagnetite (Figures 5h–5j). Samples with similar amounts of titanomagnetite and maghemite have PSD-like FORC diagrams, whereas samples with a much larger amount of maghemite than titanomagnetite have SD-like FORC diagrams (e.g., Roberts et al., 2014). Type IV samples are characterized by mixed kidney-shaped and ridge-type FORC diagrams (Figures 5k and 5l), indicating that SD hematite particles are of mixed uniaxial and triaxial magnetocrystalline anisotropy (Harrison et al., 2019; Roberts et al., 2021). SD maghemite likely contributes to the region with low B_c in the FORC distributions (e.g., Muxworthy et al., 2005).

Based on these interpretations, we reanalyze the end-member modeling results of the E_1d lavas presented in Huang, Dupont-Nivet, et al. (2015). Adopting the same three end-member (EM) model to best-interpret the IRM

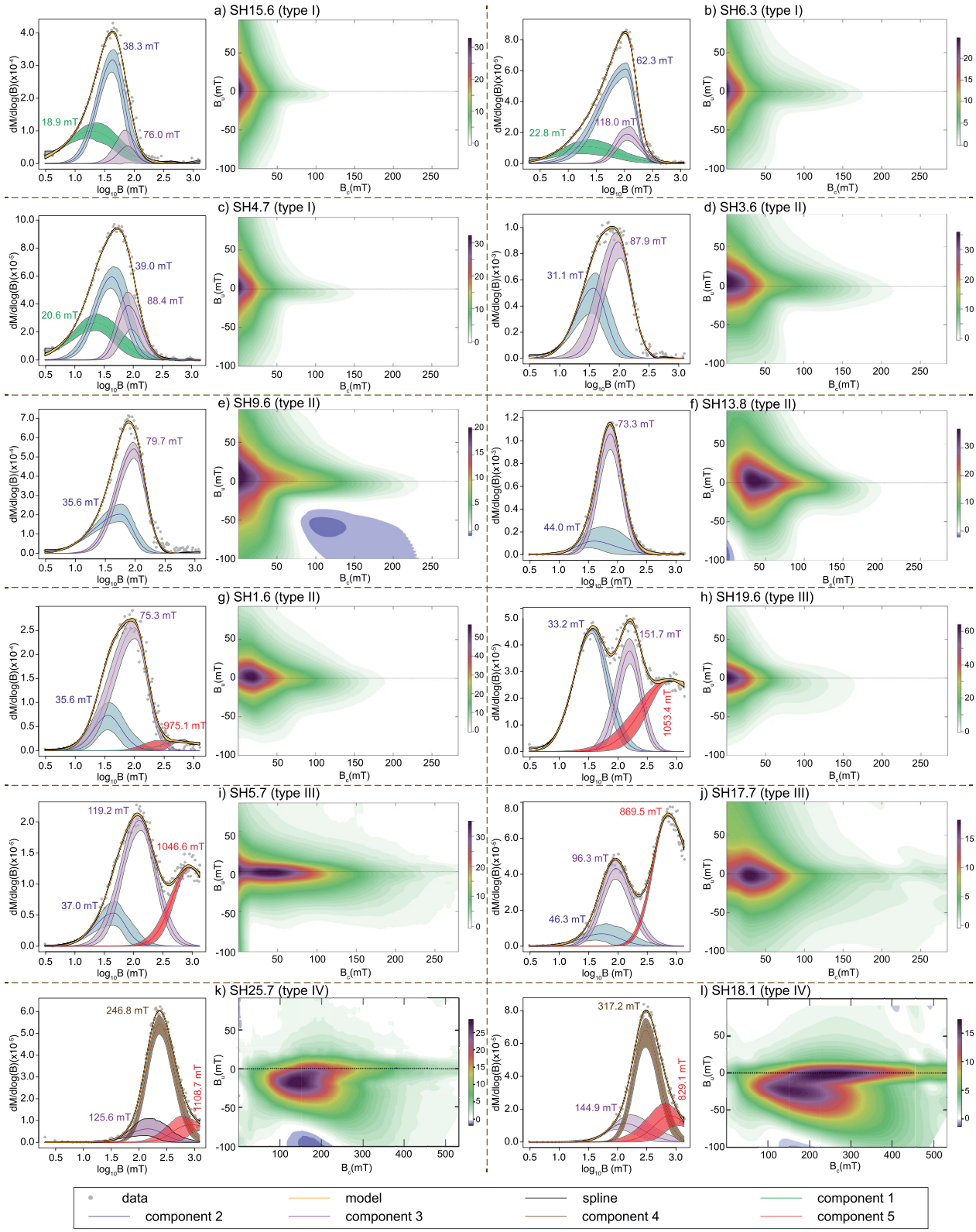

Figure 5. Component analysis of the isothermal remanent magnetization (using the Maxbauer et al. (2016) web application) and corresponding room-temperature FORC diagrams (using FORCinel V3.06 (Harrison & Feinberg, 2008)) of representative lava samples. Five components in total are used to fit the IRM acquisition curves of the lava samples. Shaded area represents error envelopes of 95% confidence intervals.

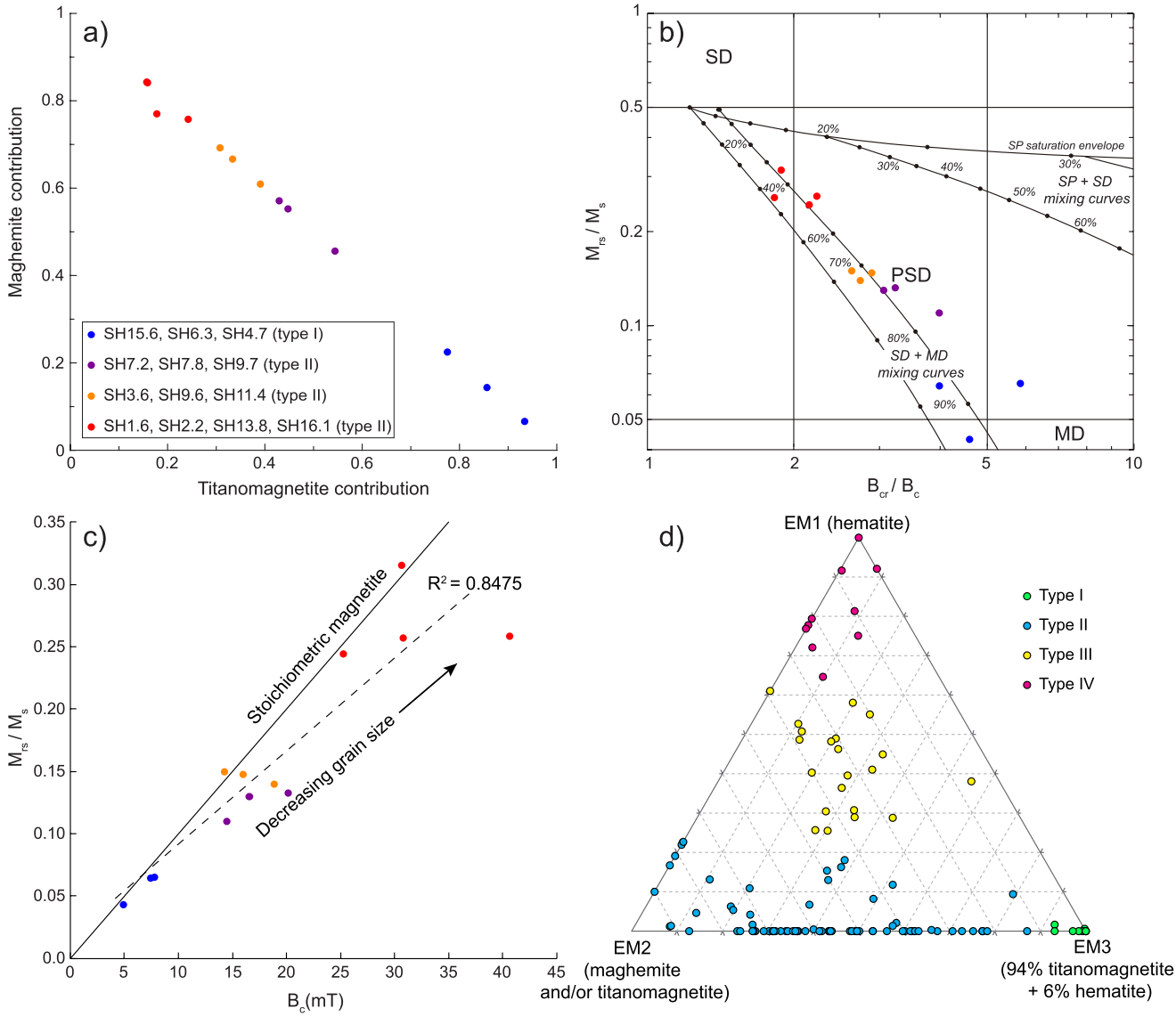

Figure 6. (a) Maghemite contribution versus titanomagnetite contribution from the IRM component analysis for the types I and II samples with little hematite. (b) Day plot of hysteresis parameters for the types I and II samples shown in (a). Note that the Day plot is not ideal for samples containing minerals other than magnetite-titanomagnetite (Roberts et al., 2018), therefore we exclude hematite-bearing types III and IV samples from the plot. SD: single domain; PSD: pseudo-single domain; MD: multidomain; SP: superparamagnetic. (c) M_{rs}/M_s versus B_c for types I–II samples shown in (a), (b). The solid line represents unoxidized stochiometric magnetite (Wang & Van der Voo, 2004). The dashed line is the least-square regression line fit through data from types I–II samples. (d) Ternary plot of the accepted three end-member model showing the end-member percentages for individual types I–IV samples modified from Huang, Dupont-Nivet, et al. (2015). The represented magnetic carriers of each endmember are reinterpreted in this study. EM2 represents maghemite for most samples, but it is dominated by PSD titanomagnetite with higher coercivity in a few type III samples. These PSD titanomagnetite grains were possibly formed by grain size reduction of magmatic MD titanomagnetite during hydrothermal alteration.

acquisition curve of 123 samples from the E_1d lavas, here we reinterpret end-member EM1 to be hematite, EM2 to be maghemite (for most samples) and/or titanomagnetite (for only a few type III samples, such as SH17.7), and EM3 to be 94% titanomagnetite plus 6% hematite. In the ternary plot of these end-members (Figure 6d), types I and II samples are distributed along or near the baseline between EM2 and EM3, type III samples are at the center of the plot, and type IV samples are close to EM1.

High-temperature hysteresis measurements of four samples (one type I, two type II, and one type III) show that M_s and M_{rs} values decrease substantially upon heating to 200°C and 500°C (Figures 4e–4h; Table S2). At 200°C, the B_c and B_{cr} values of these samples reduce noticeably, further implying that production of new magnetic minerals

(i.e., magnetite) is not the reason for the increase in susceptibility below 300°C (Figure 3). Instead, reduction of the coercivity was induced by annealing stresses within the maghemite lattice. Compared to their values at 200°C, the B_c and B_{cr} values at 500°C continue to decrease for type I sample SH15.6 and type II sample SH13.8 (Table S2 in Supporting Information S1). In contrast, these values increase in type II sample SH1.6 and type II sample SH19.6. We suggest that this is likely caused by more pronounced inversion of maghemite to hematite, as confirmed by the larger maghemite bump in these samples (Figure 3). When cooling down to the room temperature, the B_c and B_{cr} values of all samples are lower than these before the heating. We interpret this to indicate the lowering SD maghemite to MD titanomagnetite ratio, as a consequence of the transformation of maghemite to hematite during the heating experiment. This interpretation is further supported by the FORC diagrams which show that the domain states of the dominant magnetic carriers (magnetite-maghemite) in samples SH13.8 and SH1.6 change from PSD-SD before heating to PSD during and after heating, while the newly formed hematite is noninfluential in these diagrams at these concentrations owing to its much lower M_s (e.g., Muxworthy et al., 2005; Roberts et al., 2014) (Figures 4i–4p).

3.3. Low-Temperature Cycling

We first acquired the zero-field cooling and warming cycles of the room temperature 2.5 T saturation isothermal remanent magnetization (RTSIRM). In the cooling from 300 K, type I sample SH15.6 (Figure 7a) first shows a steady and gradual decrease in remanence at first, and then a sharp decrease as the specimen approaches the Verwey transition (T_V). The first derivative of magnetization versus temperature shows a T_V of 120 K, which is typical of magnetite (Verwey, 1939). Remanence of the other two type I samples (Figures 7b and 7c) at first increases slightly on cooling, reaching a maximum around 200–260 K, and then decrease quickly near the Verwey transition at 115 and 121 K. Such an increasing followed by a decreasing trend on cooling of the RTSIRM has been observed in partially oxidized magnetite (Özdemir & Dunlop, 2010). It is also mimicked by type II samples; the differences are that (a) the increase in remanence is more significant, (b) the maximum is reached at lower temperature (∼140 K), and (c) the Verwey transition is less discernible or even muted completely (Figures 7d–7f). One type II sample has a much lower T_V of 98 K (Figure 7e), which is further indication of oxidized magnetite (Jackson & Moskowitz, 2021; Kosterov, 2002; demir & Dunlop, 2010). For both types I and II samples, the cooling and warming curves are reversible for the monoclinic phase below T_V, but they are irreversible for the cubic phase above T_V. Much larger loss in RTSIRM is observed in type I samples than type II samples after temperature cycling; we attribute this to larger grain sizes in the former. The RTSIRM cooling and warming curves of a type III sample are similar to those of type II samples, but the cooling and warming curves are still spaced below the T_V and show substantial curvature with a maximum at ∼150 K (Figure 7g). The RTSIRM cooling curves of another type III sample (Figure 7h) have similarities to those of type I samples (Figure 7a), but their warming curves are completely different, with no recovery of the RTSIRM, as is their T_V (130 K). Type IV samples are characterized by continuous loss of remanence upon cooling with neither the Morin transition nor the Verwey transition identified (Figure 7i). The warming curves of these samples show an increase in magnetization, followed by a decrease at 200–240 K.

Subsequently, low-temperature 2.5 T SIRM measurements on warming in zero-field were performed after field-cooled (FC) and zero-field-cooled (ZFC) treatments. The FC and ZFC remanence of a type I sample (Figure 7a) decreases slowly before T_V, sharply across T_V, and only slightly above T_V. The FC and ZFC remanence of the other two type I samples (Figures 7b and 7c) and most type II samples (Figures 7d and 7e) decrease rapidly at 20–40 K, slowly at 40–90 K, again rapidly across the *T*v, and finally gradually from 120 K to the room temperature. Compared to the ZFC curves, the Verwey transition is more clearly identified in the FC curves. *T*v is also determined from FC curves of a type II sample where the Verwey transition is suppressed in the RTSIRM cooling curves (Figure 7f). In all type I samples and one type II sample (SH3.6), the ZFC remanence is larger than the FC remanence, indicating stronger contribution of MD grains to these remanences (e.g., Kosterov & Fabian, 2008). Both FC and ZFC curves of the type III samples show a continuous decay in remanence upon warming with visible Verwey transitions, and for the most part this behavior is not dissimilar from that of most type II samples, with the FC remanence stronger than the ZFC (Figures 7g and 7h). The FC and ZFC curves of a type IV sample SH25.7 (Figure 7i) show steady decay of the remanence with a slight manifestation of the Verwey transition, indicating the existence of a small amount of magnetite. The FC and ZFC remanence of another type IV sample SH18.1 (Figure 7j) decays quickly between 20 and 140 K, very slowly between 140 and 200 K, and very rapidly from 200 K to room temperature, indicating progressive unblocking of nanoparticles of hematite. The FC curves

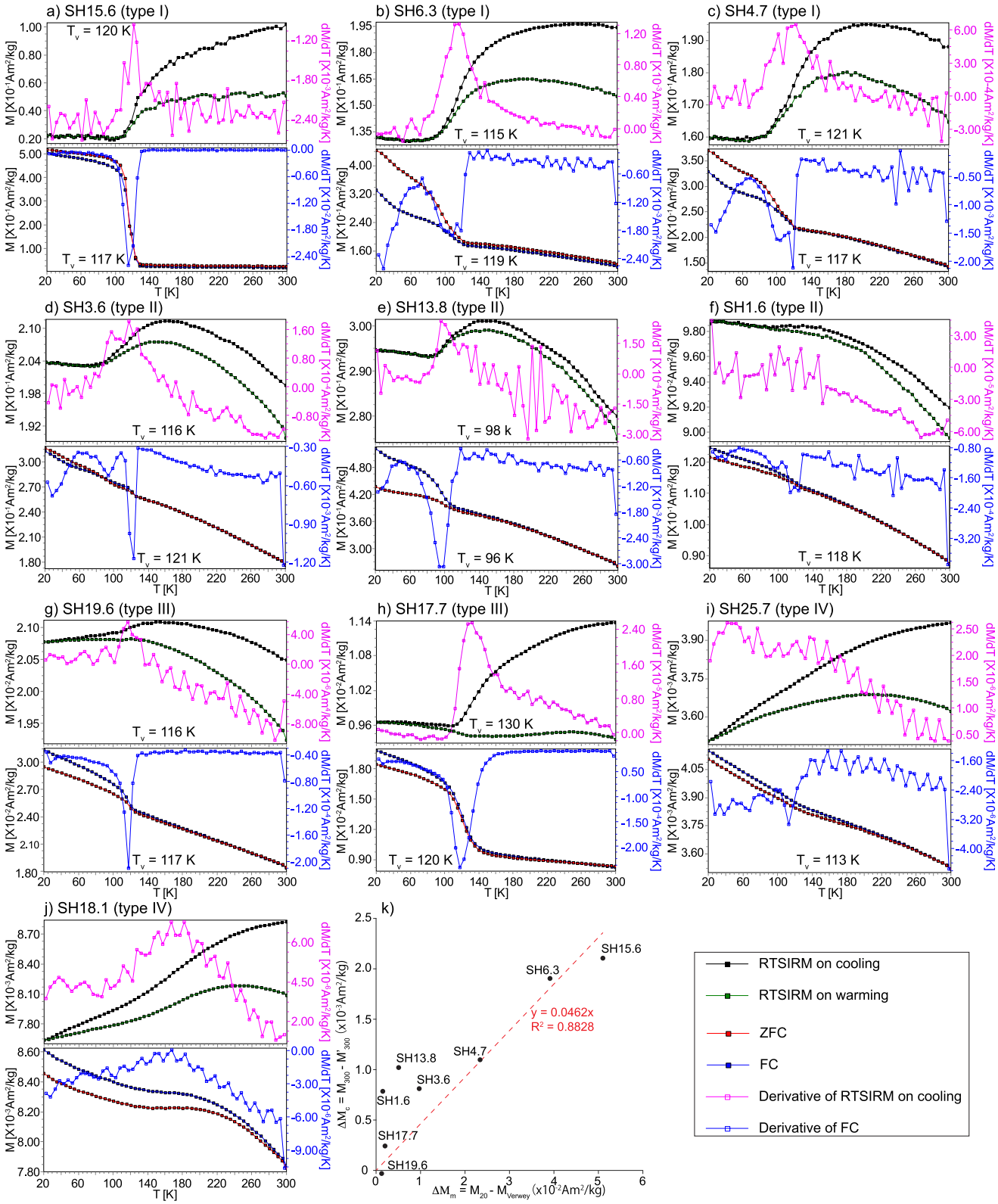

Figure 7. (a–j) Low-temperature RTSIRM cycling curves at zero field (upper), low-temperature SIRM warming curves in zero field after ZFC and FC treatments (lower), and corresponding derivatives of the RTSIRM cooling and FC curves for representative for E_1d lava samples. (k) The correlation between the parameters ΔM_c and ΔM_m determined from low-temperature RTSIRM cycling following Özdemir and Dunlop (2010). No strict linear correlation is defined from the measured samples because of the existence of hematite in most samples, but the general trend is clear that oxidation of magnetite to maghemite gets stronger toward the origin.

of these two type IV samples are higher than their ZFC curves, which together with the spacing of the two curves until ~180 and 300 K, is indicative of nano- and more crystalline goethite, respectively (Guyodo et al., 2003).

Stoichiometric magnetite has a sharp transition across T_V and permanent remanence loss after the RTSIRM cooling and warming cycles, whereas pure maghemite has no Verwey transition and reversible RTSIRM cooling and warming curves (Özdemir & Dunlop, 2010). Therefore, the low-temperature measurements reveal that (titano)magnetite in type I samples were slightly oxidized to maghemite. In contrast, the hump shaped RTSIRM cooling and warming curves above T_V, the broadened or even suppressed Verwey transition, and the shift of the Verwey transition to lower temperature, consistently indicate that type II samples were strongly to nearly completely oxidized to maghemite. The large amount of hematite identified in type III samples and the similar low-temperature cycling features of one type III sample (SH19.6) and the type II samples, indicate a mixture of titanomagnetite and maghemite. Another type III sample (SH17.7) has similar low-temperature behavior to the slightly oxidized type I sample, confirming the existence of titanomagnetite in addition to hematite.

To investigate the oxidation parameter of titanomagnetite in types I–III samples, we tentatively plot ΔM_c versus ΔM_m (Figure 7k), where ΔM_c (= M_{300}-M'_{300}) is the remanence lost at 300 K before and after zero-field cooling and warming cycles for the cubic phases above the T_V, and ΔM_m (= M_{20}-M_{Verwey}) is the remanence lost between 20 K (the lowest measuring temperature) and Verwey temperature in the zero-field warming curves for monoclinic magnetite below the T_V (Özdemir & Dunlop, 2010). Although the parameters ΔM_c and ΔM_m are not strictly proportional to each other due to the existence of hematite in some samples, there is a general trend indicative of increasing oxidation of titanomagnetite to maghemite toward the origin in the plot. The slope of the linear least-squares fit is very different from that of the 220 and 37 nm partially oxidized magnetite (Özdemir & Dunlop, 2010), possibly caused by the larger titanomagnetite grain size in our samples.

3.4. Mössbauer Spectroscopy

Mössbauer spectroscopy has traditionally been used to determine Fe^{3+} and Fe^{2+} in geologic samples. We obtained Mössbauer spectra from SH15.6 (type I) at 295 K and SH13.8 (type II) at both 295 and 18 K. The magnetic hyperfine parameters and the relative proportion of each component determined from the spectra are presented in Table S4 in Supporting Information S1. Bulk hematite has a respective magnetic hyperfine field (B_{HF}) of 51.8 T at room temperature and of 54.2 T at 4.2 K (Murad & Cashion, 2004). Pure magnetite has a B_{HF} of 49.0 T for Fe^{3+} in tetrahedral sites and a B_{HF} of 46.0 T for Fe^{3+} and Fe^{2+} in octahedral sites at room temperature, and a B_{HF} of 51.5 T for Fe^{3+} in tetrahedral sites and a mean B_{HF} of 48.9 T for Fe^{3+} and Fe^{2+} in octahedral sites at 4 K (Doriguetto et al., 2003; Dyar et al., 2006). Mössbauer spectra for titanomagnetite is very sensitive to Ti concentration: titanomagnetite ($Fe_{3-x}Ti_xO_4$) with $x < 0.1$ has the characteristic two-sextet pattern of pure magnetite with slightly lower B_{HF} of 48.8 T for tetrahedral sites and 45.8 T for octahedral sites (e.g., Lipka et al., 1988). Bulk maghemite is fitted with two strongly overlapping sextets from Fe^{3+} in tetrahedral and octahedral sites at room temperature with the B_{HF} of 49.9 T; the B_{HF} is 52.0 T in tetrahedral sites and 53.1 T in octahedral sites at 8 K (Da Costa et al., 1995; Dyar et al., 2006).

The Mössbauer spectrum at 295 K for bulk sample SH15.6 can be fitted with three sextets and three doublets (Figure 8a). The minor sextet with the highest B_{HF} of 51.4 T is like that of hematite at room temperature. The main sextet has the lowest B_{HF} of 45.9 T, representing Fe^{3+}, Fe^{2+}, and trace amounts of Ti^{4+} in octahedral sites in titanomagnetite. The sextet with B_{HF} of 48.9 T represents Fe^{3+} in tetrahedral sites in titanomagnetite and in tetrahedral and octahedral sites in maghemite. Modeling of the spectra indicates that ~3.90% of the iron resides in hematite, ~16.29% of the iron resides in tetrahedral sites in titanomagnetite and in tetrahedral and octahedral sites in maghemite, and ~26.57% of iron resides in octahedral sites of titanomagnetite; the remaining iron is in paramagnetic or superparamagnetic particles. Because tetrahedral iron is half of octahedral iron in magnetite, the contribution of tetrahedral iron in titanomagnetite should be ~13.29%. Thus, the amount of iron residing in maghemite at room temperature should be ~3.00%.

We fitted the Mössbauer spectrum at 295 K for bulk sample SH13.8 with three sextets and three doublets (Figure 8b). The sextet with the highest B_{HF} of 51.2 T represents hematite. The minor sextet has the lowest B_{HF} of 45.6 T, and possibly reflects Fe^{3+}, Fe^{2+}, and small amounts of Ti^{4+} in octahedral sites in titanomagnetite. We interpret the sextet with B_{HF} of 49.4 T to be a mixture of Fe^{3+} in tetrahedral sites in titanomagnetite and Fe^{3+} in tetrahedral and octahedral sites in maghemite. Modeling of the spectra suggests that hematite has a high

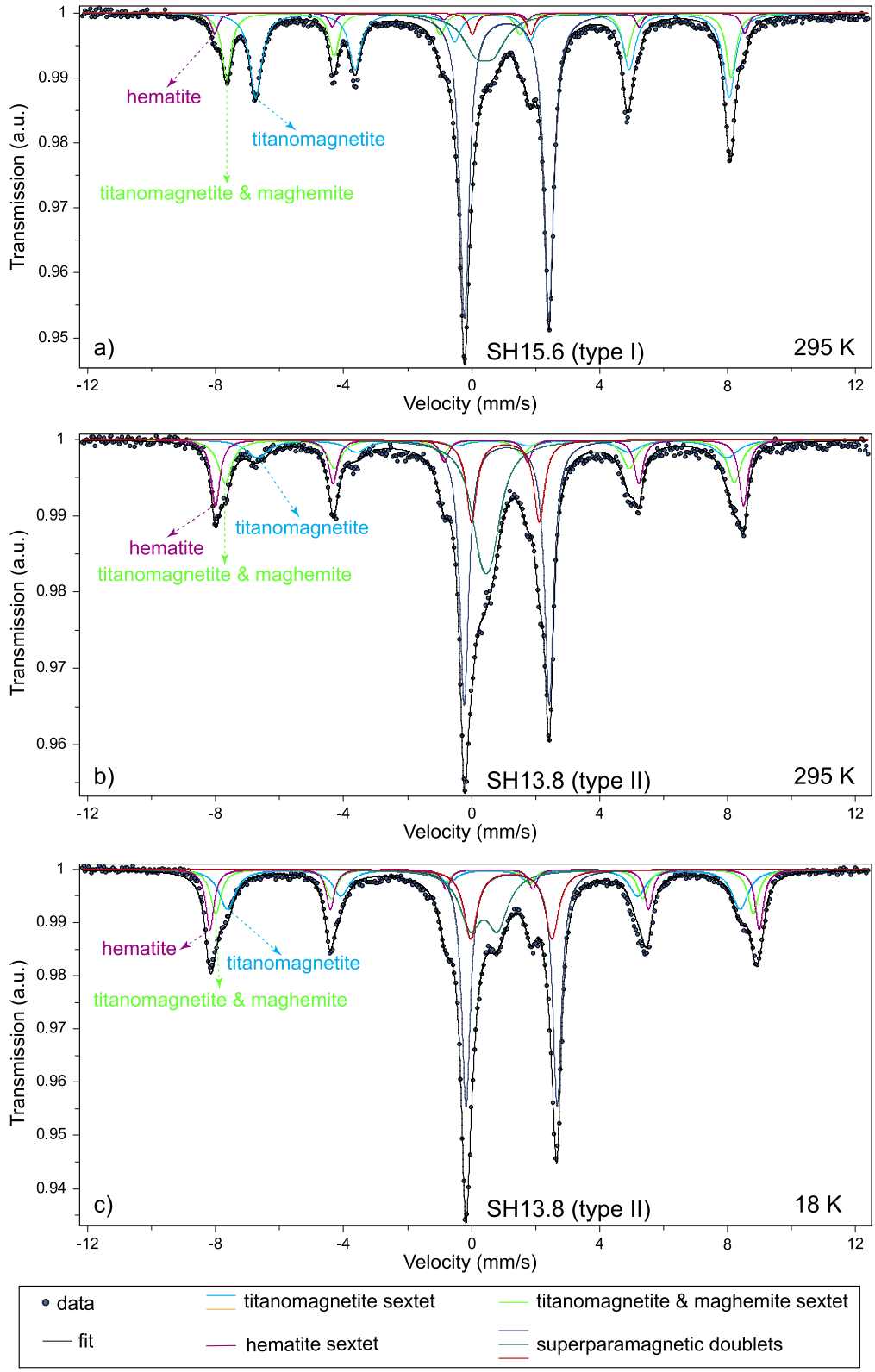

Figure 8. Mössbauer spectrum for a type I sample SH15.6 (a) at 295 K and a type II sample SH13.8 at both 295 K (b) and 18 K (c). Dots with the black lines are data and model fits. Purple sextets are the fits diagnostic of hematite; green sextet represents tetrahedral iron in titanomagnetite, and tetrahedral and octahedral iron in maghemite; blue sextet is representative of octahedral iron and little titanium in titanomagnetite. The central peaks are composed of superposed doublets dominated by Fe^{3+}.

contribution of 14.32%, octahedral iron and little titanium in titanomagnetite has a contribution of 10.13%, and iron in tetrahedral site in titanomagnetite and iron in tetrahedral and octahedral sites in maghemite have a net contribution of 14.66%. Based on the stoichiometric requirement that tetrahedral iron is half that of octahedral iron in magnetite, we estimate the contribution of tetrahedral iron in titanomagnetite to be ~5.07%. Therefore, the total iron residing in titanomagnetite is ~15.20%, and ~9.60% of iron should reside in maghemite in this sample at 295 K.

For bulk sample SH13.8, the Mössbauer spectrum at 18 K can also be fitted with three sextets and three doublets (Figure 8c). The sextet with the highest B_{HF} of 53.4 T is interpreted to be hematite. The sextet with lowest B_{HF} of 49.9 T represents octahedral iron and little titanium in titanomagnetite, and the sextet with B_{HF} of 52.3 T possibly represents iron in maghemite and tetrahedral iron in titanomagnetite. Modeling of the spectra reveals that 13.4% of iron resides in hematite, octahedral iron and little titanium in titanomagnetite has a contribution of 17.8%, and iron in tetrahedral site in titanomagnetite and iron in tetrahedral and octahedral sites in maghemite have a net contribution of 12.7%. In the same way, we calculate that iron residing in titanomagnetite and maghemite is 26.7% and 3.8%, respectively, indicating that a large amount of (titano)magnetite is superparamagnetic at 295 K but is blocked at 18 K in this sample.

3.5. Microscopy

We made SEM observations (Figures 9 and 10) and associated EDS analyses (Figure S1, Table S5 in Supporting Information S1) to identify textural and chemical properties of the magnetic carriers in the E_1d lavas. This leads to an estimate of their transformation related to alteration. The dominant magnetic phase in the type I samples is unaltered euhedral to subhedral Ti-poor titanomagnetite with grain size varying from 1 μm to >100 μm (Figures 9a and 9b). Solid-state oxidation-exsolution features with ilmenite lamellae distributed in the Ti-poor magnetite can be observed (Figure 9b). Shrinkage cracks, formed to accommodate the decrease in lattice parameters with oxidation, are observed in some titanomagnetite grains, suggesting that these grains have been partially oxidized to maghemite (Figure 9c). These altered grains are often cut by thin hematite veins (Figure 9c). In the type II samples (Figures 9d–9i), shrinkage cracks are ubiquitous, indicating significant oxidation of the titanomagnetite grains. These titanomagnetite grains also show evidence of alteration with iron leached from the lattice and pores created in the lattice; this is supported by their lower Fe concentration as indicated by the EDS analysis (Figure S1, Table S5 in Supporting Information S1). The alteration is possibly related to the hematite veins penetrating these grains: the most intense alteration is often observed in areas immediately adjacent to the veins. Moreover, fine hematite grains are found surrounding the oxidized titanomagnetite (Figures 9c–9i). In a type III sample (Figures 10c and 10d), we observed the replacement of titanomagnetite by amorphous Ti-rich material distributed along the shrinkage cracks of preexisting titanomagnetite. The residual titanomagnetite has been strongly oxidized and extensively penetrated by hematite veins. Authigenic hematite is also observed around or within the titanomagnetite grains (Figures 10e and 10f). In type IV samples, hematite is widespread and mostly porous. Aggregates of tiny dendritic and flake-like hematite grains pseudomorphic after titanomagnetite are observed (Figures 10g and 10i). Some hematite grains are filling the cracks or pores within or between silicate crystals (Figures 10g and 10h). EDS analysis reveals that hematite grains have much lower Ti concentration than the titanomagnetite grains (Figure S1, Table S5 in Supporting Information S1).

4. Discussion

4.1. Magnetic Minerals and Their Formation in the E_1d Lavas

Rock magnetic experiments (Figures 3–7), Mössbauer spectroscopic measurements (Figure 8), and SEM observations and EDS analyses (Figures 9 and 10, Figure S1 in Supporting Information S1) on the E_1d lavas consistently indicate that magnetic carriers in the types I–IV samples vary as function of alteration (Figure 11); here alteration is ascribed based on color of the rocks and visual inspection of the thin sections. For slightly altered type I samples, the dominant magnetic carrier is MD titanomagnetite with accessory magnetic SD maghemite. A small amount of hematite was also identified by Mössbauer spectroscopy (Figures 8a and 11b), but its contribution to the remanence is negligible because the saturation magnetization of hematite is 1/200 that of magnetite (e.g., Roberts et al., 2021, and references therein). For moderately altered type II samples, MD titanomagnetite and SD maghemite are the dominant magnetic carriers, while SD hematite is the minor magnetic carrier

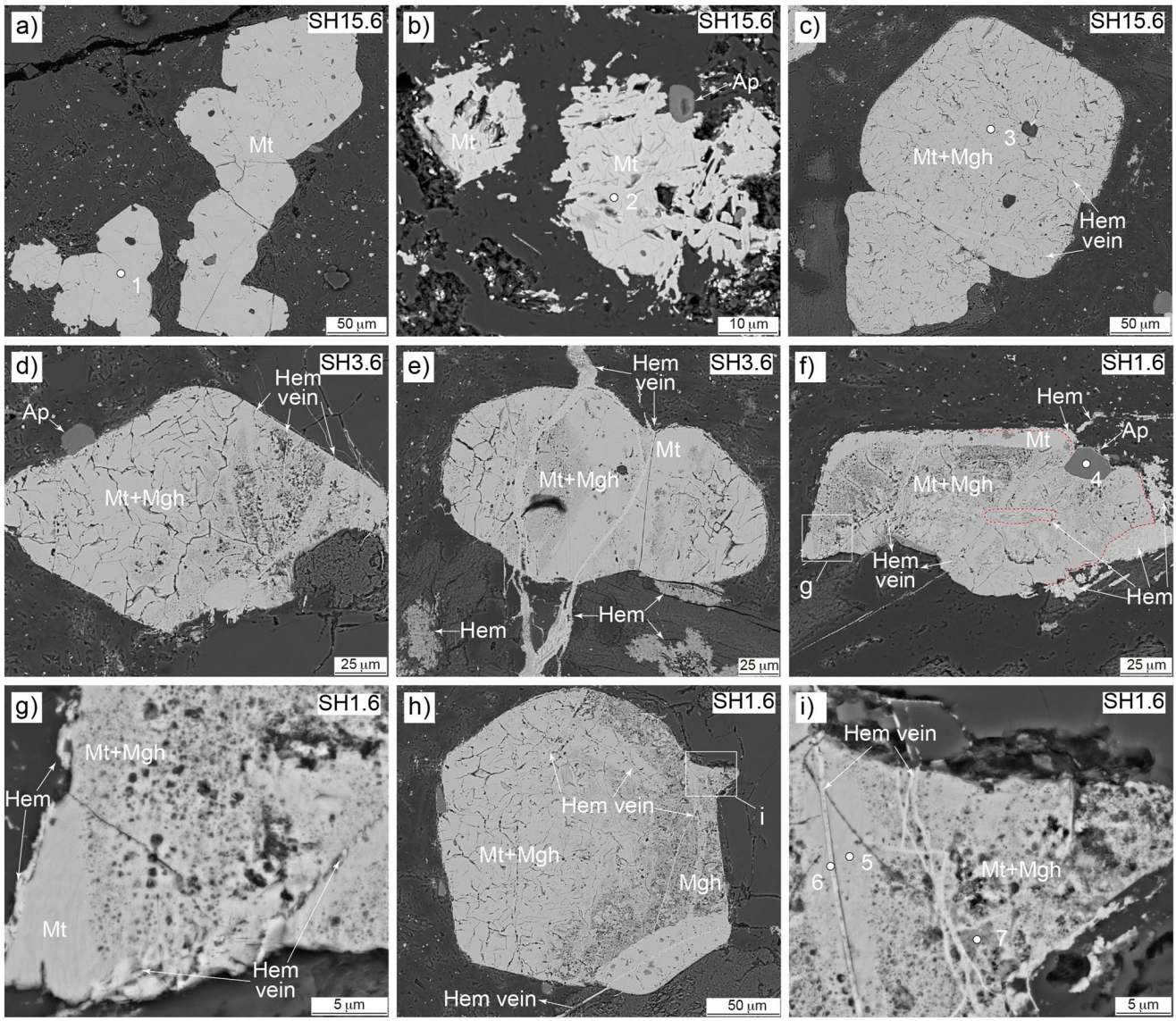

Figure 9. SEM backscattered electron images of types I and II samples from the E_1d lavas. SH15.6 (a–c) is a type I sample; SH3.6 (d–f) and SH1.6 (g–j) are type II samples. Mt: titanomagnetite; Mgh: maghemite; Hem: hematite; Ap: apatite. Dots are spots for EDS analysis, the results are presented in Figure S1and Table S5 in Supporting Information S1.

(Figure 11c). For strongly altered type III samples, SD hematite is abundant, and the concentrations of PSD-MD titanomagnetite and SD maghemite vary widely among samples (Figure 11d). In nearly completely altered type IV samples, SD hematite has extremely high concentration (in terms of magnetic moment) with >85% of remanence residing in it; SD maghemite is only minor, and titanomagnetite is very little (Figure 11e). The characterization of the morphological and textural features indicates that titanomagnetite in the E_1d lavas has a magmatic origin, whereas maghemite and hematite are authigenic (Figures 9 and 10). From type I to type IV samples, SEM observations show that the relative abundance of titanomagnetite decreases, while that of maghemite and hematite increase (Figures 9 and 10). These observations are consistent with rock magnetic results showing that magnetic susceptibility, and NRM and IRM intensities of types III and IV samples are ~100 times weaker than those of types I and II samples (Figures 2–7). The formation of maghemite and hematite occurs thus at the expense of titanomagnetite.

Under both dry and aqueous conditions, oxidation of magnetite $[Fe^{2+}(Fe^{3+})_2(O^{2-})_4]$ starts at the grain's surface and along the microcracks, it continues through outward diffusion of Fe^{2+} driven by the oxidation gradient (e.g., Ge et al., 2014; Tang et al., 2003). Such a solid-state diffusion process leaves behind vacancies in the interior

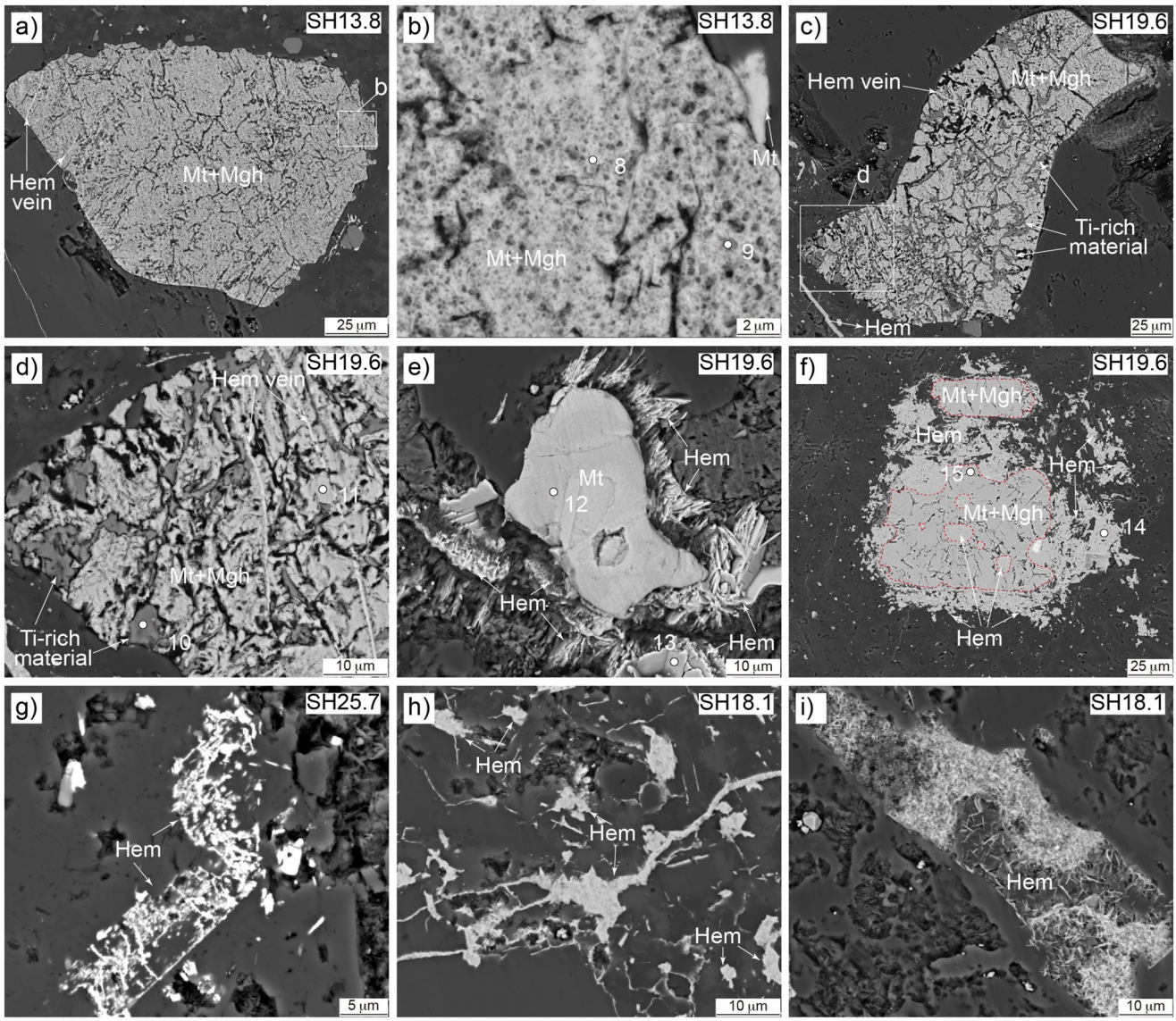

Figure 10. SEM backscattered electron images of types III and IV samples from the E_1d lavas. SH13.8 (a), (b) and SH19.6 (c)–(f) are type III samples; SH25.7 (g) and SH18.1 (h)–(i) are type IV samples. Mt: titanomagnetite; Mgh: maghemite; Hem: hematite; Ap: apatite. Dots are spots for EDS analysis, the results are presented in Figure S1 and Table S5 in Supporting Information S1. Red dashed lines represent the boundary between magnetite/maghemite and hematite.

and leads to formation of a maghemite [γ- $(Fe^{3+})_2(O^{2-})_3$] shell (Figure 11) around the unoxidized magnetite core (e.g., Housden & O'Reilly, 1990). The liberated Fe^{2+} at the surface or magnetite-maghemite interface is either partially removed from the crystal or it reacts with oxygen. The solid-state diffusion coefficient of Fe^{2+} and the inversion rate of magnetite to maghemite depend strongly on temperature, the diffusion rate at 150°C is 12 orders of magnitude higher than that at 30°C (Askill, 1970; van Velzen & Zijderveld, 1995). Thus, oxidation is very slow at room temperature with respect to geologic times but can be very rapid at elevated temperature. Likewise, the magnetite grain size also controls the reaction speed: oxidation rates increase with larger surface/volume ratios. Petrographic and thermochronologic studies indicate that the E_1d lavas have experienced two hydrothermal events, leading to hydrothermal alteration with concomitant heating: to ~300°C at ~52 Ma and ~130–145°C at ~42–27 Ma (Huang et al., 2015a, 2022). We hypothesize that the heating induced rapid diffusion of Fe^{2+} from the interior of the titanomagnetite grain to the surface or magnetite-maghemite interface. The widespread occurrence of hematite veins cutting the titanomagnetite grains (Figures 9 and 11b) suggests that the oxidation of titanomagnetite was related to hydrothermal fluids. Shrinkage cracks and pores within the titanomagnetite crystals (Figures 9 and 11b) create permeability and reduce the isolation effect of the oxidized maghemite layer:

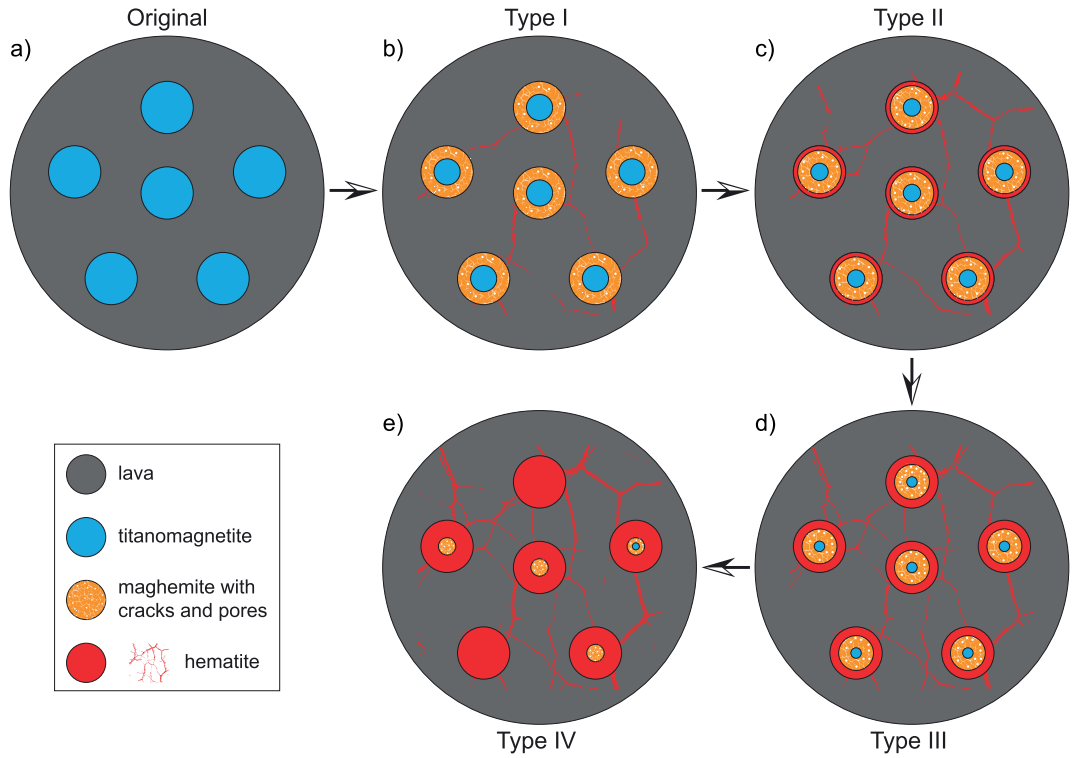

Figure 11. Transformation of magnetic minerals within the E_1d lavas with increasing high-temperature hydrothermal alteration. (a) The original magnetic carrier in the E_1d lavas was multi-domain Ti-poor titanomagnetite; the primary remanent magnetization was acquired when the magma was cooling through the Curie temperature of titanomagnetite; (b) In slightly altered type I samples, a single-domain maghemite shell surrounding the titanomagnetite core was formed due to solid-state diffusion of Fe^{2+} out of titanomagnetite lattice, part of the liberated Fe^{2+} reacted with oxygen in solution and deposits as hematite vein; The TVRMs residing in titanomagnetite and the CRMs residing in maghemite/hematite were acquired, the primary remanence was partially replaced and contaminated by secondary remanence. (c) In moderately altered type II samples, titanomagnetite transformed to maghemite extensively, hematite was formed around the titanomagnetite/maghemite, or filling the cracks and pores within the lavas; intensity of the primary remanence was significantly reduced with the increasing acquisition of the TVRMs and CRMs. (d) In strongly altered type III samples, titanomagnetite largely inverted to maghemite and hematite; the primary remanence was strongly destroyed and replaced by the TVRMs and CRMs. (e) Magnetic carriers in the (nearly) completely altered type IV samples are hematite and minor maghemite, titanomagnetite is rarely preserved; the primary remanence has been (nearly) completely replaced by the CRMs. The magmatic titanomagnetite experiences significant grain size reduction with domain state changing from multi-domain (a), (b) to pseudo-single domain and single-domain (c)–(e). The authigenic maghemite and hematite are in single-domain state (b)–(e). The southern margin of Asia was located at ~23–30°N during the hydrothermal events at 52 Ma and 42–27 Ma, the TVRMs and CRMs would be 180°/–40°–180°/–49° (Declination/Inclination) in direction. The isolated ITC/HTC direction of the Dianzhong lavas is D_g/I_g = 195.9°/–25.4° before the tilt correction and D_s/I_s = 193.5°/–11.6° after tilt correction (Huang, Dupont-Nivet, et al., 2015). Acquisition of the TVRMs and CRMs thus occurred when the E_1d lavas were tilted to the north with the dip of ~28–38°, which is >12–22° steeper than that of today (the current bedding attitude is dip azimuth/dip = 9.2°/16.6° for the lower E_1d and dip azimuth/dip = 339°/15.2° for the upper E_1d, Huang, Dupont-Nivet, et al. (2015)). The TVRMs and CRMs thus have shallower inclination (11.6°) than that of the primary remanence (36°, assuming a paleolatitude of 20°N during the E_1d eruption, Lippert et al. (2014)) in stratigraphic coordinates, and this is resulted from mistaken tile correction applied to secondary magnetization (TVRM and CRM) acquired after tilting of the bedding. Acquisition of both the primary remanence and TVRMs by titanomagnetite and overlapping of the unblocking/inversion temperature spectra of the authigenic maghemite/hematite with those of the titanomagnetite imply that the ITC isolated in the E_1d lavas is a combination of the primary remanence, TVRMs, and CRMs, and the HTC is the CRMs. This explains the shallower and similar directions of the ITC and HTC from the four types of the E_1d lavas.

this leads to efficient transport of liberated Fe^{2+} ions away from the titanomagnetite crystal. These Fe^{2+} ions were oxidized and deposited as hematite. Consequently, heating and fluid circulation during such events provide a viable mechanism for the severe oxidation of titanomagnetite to maghemite observed in the E_1d lava.

The transformation of magnetite to hematite can occur through solid-state oxidation by molecular O_2 following Equation (1) (Davis et al., 1968; Dunlop & Ödemir, 1997). It can also proceed via non-redox interface-coupled

dissolution-reprecipitation reaction in hydrothermal systems following Equations (2) and (3) (e.g., Ohmoto, 2003; Otake et al., 2007; Yin et al., 2022; Zhao et al., 2019).

$$4Fe_3O_4\ (\text{magnetite}) + O_2 = 6Fe_2O_3\ (\text{hematite}) \quad (1)$$

$$Fe_3O_4\ (\text{magnetite}) + 2H^+ = Fe_2O_3\ (\text{hematite}) + Fe^{2+} + H_2O\ (\text{acidic conditions}) \quad (2)$$

$$Fe_3O_4\ (\text{magnetite}) + H_2O = Fe_2O_3\ (\text{hematite}) + Fe^{2+} + 2OH^-\ (\text{basic conditions}) \quad (3)$$

The redox reaction involves formation of maghemite and subsequent gradual inversion of maghemite to hematite and is associated with a slight volume increase of 1.66% (Davis et al., 1968). In contrast, the non-redox reaction involves leaching of Fe^{2+} from magnetite, formation of ferrihydrite and its successive transformation to goethite and hematite and is characterized by a significant volume decrease of ~32% (Ohmoto, 2003). SEM observations of samples from the E_1d lavas show that the authigenic hematite is porous (Figures 10e, 10g–10i). Formation of these pores may be related to volume decrease in non-redox reactions (Xing et al., 2021). Our rock magnetic studies reveal the existence of maghemite in types I–IV samples and goethite in type IV samples (Figures 3–8). Moreover, the E_1d lavas have experienced two hydrothermal events, leading to extensive hydrothermal alterations (Huang et al., 2022). Therefore, considering that the E_1d lavas were buried by the overlying Linzizong strata to a depth of ~3 km where the availability of oxidant (O_2) is very low, we suggest that the non-redox reaction path has been the main mechanism for the formation of hematite. That said, some redox reaction may also have been involved, evidenced by the hematite veins.

In natural rocks at depth, the fluid/rock ratio is small. As such, the rate-limiting process for the magnetite to hematite transformation is the efficiency of Fe transport, which depends on the presence of fluid availability and permeability of the rocks. Dissolution of magnetite at the reaction front releases both Fe^{3+} and Fe^{2+}, the Fe^{3+} instantly precipitates and forms hematite, owing to its low solubility and nucleation facilitated by existing mineral surfaces (Yin et al., 2022). This can explain the observed formation of hematite around the titanomagnetite and maghemite grains (Figures 9f–9h and 9j, 9o–9p; 11c–11d). However, insufficient oxygen at the reaction front likely leads to transportation of the more soluble Fe^{2+} from the reaction front through cracks and pores: these Fe^{2+} ions then can react with O_2 in the solution (i.e., penetrating rainwater or groundwater) to form hematite filling the cracks, pores, and voids within/between the titanomagnetite and silicate crystals (Figures 9c–9t; 11b–11e). The shrinkage cracks related to maghemitization and the pores created by Fe^{2+} leaching and titanomagnetite dissolution (Figures 9 and 11) enhance the rock's permeability, which leads to efficient mass transport between the reaction front and the fluid and keeps the interfacial fluid unsaturated, further promoting the reaction and driving the replacement (Zhao et al., 2019). Temperature is another potential controlling factor for the transformation as the reaction rate typically increases with temperature. Although magnetite equilibrium solubility would decrease with increasing temperature, this is generally counterbalanced by high diffusion coefficients and faster dissolution kinetics at high temperatures (Zhao et al., 2019). Besides, both transformation from ferrihydrite to hematite and dehydration of goethite to hematite is favored at high temperature (e.g., Yapp, 1990). Other factors, including oxygen fugacity, pH, and the Cl^- and dissolved silica concentrations of the fluid might also shape the pathway for hematite growth (Yin et al., 2022). For example, although the absence of O_2 has little effect on the non-redox reaction, laboratory studies show that oxidant addition may trigger the oxidation reaction under mild hydrothermal conditions (140–220°C), resulting in formation of additional hematite (Zhao et al., 2019).

In summary, we argue that the original titanomagnetite grains of magmatic origin in the E_1d lavas have been variably transformed to authigenic maghemite and hematite due to hydrothermal alteration. At the sample level, maghemitization and hematization were most likely controlled by circulation of high-temperature hydrothermal fluid. Hydrothermal fluid migrated thoroughly through lavas close to the dikes and near the unconformity between E_1d and E_2n and induced the strong hematization of types III and IV samples (Figures 1; 11daysay, e). In contrast, migration of hydrothermal fluid through types I and II samples was less pervasive, leading to maghemitization of titanomagnetite within these rocks (Figures 11b and 11c). The titanomagnetite grain size had a major effect on the maghemitization and hematization. In the types II and III samples, smaller titanomagnetite grains are observed to invert to hematite, but larger titanomagnetite grains are strongly oxidized to fine-grained maghemite (Figures 9c–9e).

4.2. Origins of the NRM in the E_1d Lavas

Based on the rock magnetic experiments, petrographic observations, and interpretations for the formation of magnetic minerals, we first discuss the NRMs residing in each magnetic carrier and then characterize the nature

of the low, intermediate, and high temperature components of each NRM. Our analysis shows that MD titanomagnetite is the original magnetic carrier in the E_1d lavas. This MD titanomagnetite acquired a primary remanence during the cooling below its Curie temperature during lava emplacement. However, both the titanomagnetite and this primary remanence have been modified during the subsequent hydrothermal events. Hydrothermal event I, induced by extensive intrusion of dikes in the E_1d and E_2n and massive ignimbrite eruption in E_2p, heated the E_1d strata up to 300°C for 1 million years (Myr) (Huang et al., 2022). Considering that the Curie temperatures for titanomagnetite in the E_1d samples are 549–568°C (Figure 3), the MD theory of titanomagnetite (Berndt & Chang, 2019) predicts that such heating could reset the primary remanence for all grains whose unblocking temperature is below 450°C in the laboratory; this would induce the acquisition of a thermoviscous remanent magnetization (TVRM1). Similarly, MD theory also predicts that hydrothermal event II, during which the E_1d lavas were heated to 130–145°C for 1 Myr (Huang et al., 2022), could result in replacement of the portion of TVRM1 that unblocks below 300–350°C by a new TVRM (TVRM2).

Hydrothermal events also induced the inversion of titanomagnetite to maghemite and hematite, erasing the primary remanence and/or TVRM carried by titanomagnetite and leading to the acquisition of CRMs carried by authigenic maghemite and hematite. Maghemite preserves the remanence direction of the precursor titanomagnetite because of the superexchange coupling between titanomagnetite and maghemite (e.g., Özdemir & Dunlop, 1985), implying that maghemite CRMs could be coaxial with the primary remanence, TVRM1 and TVRM2. Hematite CRMs would instead record the field direction that prevailed during the TVRM1 and/or TVRM2 events.

To characterize the LTC properties from the E_1d lavas, we compare the demagnetization diagrams of types I–IV samples. One of the most remarkable phenomena in these demagnetization diagrams is the difference in the extent of the LTC: a very strong LTC can be isolated from types I and II samples, a relatively weak LTC is determined in type III samples, but the LTC is entirely missing in type IV samples (Figure 2). Considering that the LTC is typically isolated below 300°C and that the concentration of titanomagnetite reduces significantly from dominance in type I samples to absence in type IV samples, it is very likely that the LTC has a thermoviscous origin and resides in MD titanomagnetite. The mean direction of the LTC ($D_g/I_g = 0.8°/41.1°$, $k = 11.7$, $\alpha_{95} = 4.8$) deviates from the geocentric axial dipole field direction ($D/I = 0°/49.1°$) for the present latitude, indicating that it cannot be a recently acquired thermoviscous overprint (Huang, Dupont-Nivet, et al., 2015). We suggest that it represents the TVRM2 acquired while E_1d was cooling after peak heating to 130–145°C during hydrothermal event II (Huang et al., 2022). This hypothesis is supported by the consistence of the temperature range (<300°C) over which the LTC is isolated, and with the MD theory-predicted unblocking temperature range (<300–350°C) for the TVRM2 (Berndt & Chang, 2019).

The χ–T curves indicate that the Curie temperatures for titanomagnetite, maghemite, and hematite in the E_1d samples are 549–568°C, 591–604°C, and 658–665°C (Figure 3), respectively. Combined with the observations that maghemite inverts to hematite between 300 and 500°C shown by the χ–T curves (Figure 3) and that fine-grained authigenic hematite (120–200 nm in diameter) has lower unblocking temperatures (300–580°C) (Swanson-Hysell et al., 2019) than the Curie temperatures of magnetite, the ITC (isolated at 350–580°C) in the E_1d lavas has a complex origin. For type I samples whose magnetic mineralogy is dominated by titanomagnetite and maghemite, the ITC likely represents a combination of primary remanence and TVRM1 residing in titanomagnetite, and CRMs residing in maghemite. For type II samples, the ITC is carried by maghemite, titanomagnetite, and small amounts of fine-grained hematite. It is thus a combination of CRMs residing in maghemite, primary remanence and TVRM1 residing in titanomagnetite, and the small amount of CRM residing in hematite. For type III samples, the ITC resides in fine-grained hematite, maghemite, and titanomagnetite, and is thus a combination of CRMs residing in hematite and maghemite, primary remanence and TVRM1 residing in titanomagnetite. For type IV samples, the ITC resides in fine-grained hematite and maghemite, and thus represents the CRM. Moreover, for the HTC isolated at >580°C in types II–IV samples, the magnetic carriers are maghemite and hematite; the HTC thus records the CRM direction.

Of all the TVRMs and CRMs acquired during the hydrothermal events, only the TVRM2 has a well-determined LTC direction. Overlapping of the unblocking temperature ranges of magmatic titanomagnetite and authigenic maghemite and hematite suggest that neither the ITC nor the HTC of types I–IV samples is a pure primary remanence. It is also difficult to speculate on the potential directions of TVRM1 and each CRM because the bedding attitude of the E_1d lavas during acquisition of these secondary remanence is unknown. The final directions of

the HTC and ITC in the E_1d lavas depend on the concentrations of the specific magnetic minerals carrying these remanences, and their recorded directions and polarities. Moreover, even the same type of authigenic magnetic minerals might have formed at different times (e.g., during different hydrothermal events) and thus carry remanence with distinct directions and polarities. Timing the acquisition of secondary remanent magnetizations (TVRMs and CRMs) in the E_1d lavas is crucial for the understanding the whole remagnetization process. This task can be accomplished by linking the thermal history of the E_1d lavas to the TVRM acquisition and by direct-dating of the secondary magnetic minerals carrying the CRM, which will be the focus of a future study.

4.3. Implications for Modification of the Primary Remanence by Hydrothermal Alteration

Hydrothermal alteration is one of the main reasons for the modification of magnetic mineralogy and the NRM in submarine and subaerial rocks (e.g., Elmore et al., 2012; Font et al., 2012; Kontny et al., 2003; Oliva-Urcia et al., 2011). Previous investigation of sea floor weathering indicates that interaction of the oceanic basalt with low-temperature sea water or hydrothermal fluids induces widespread oxidation of titanomagnetite to titanomaghemite, leading to a decrease of NRM intensity. Sometimes oxidation progresses to acquisition of a self-reversed CRM, with the primary thermoremanent magnetization well-preserved (e.g., Doubrovine & Tarduno, 2006; Fabian & Shcherbakov, 2020; Matzka et al., 2003). In contrast, recent studies on oceanic basalt from the bleached zones in active spreading ridges reveal that these rocks experienced destructive high-temperature hydrothermal alteration, characterized by formation of secondary magnetite through recrystallization of exsolved and dissolved Fe from primary titanomagnetite. Significant reduction of NRM intensity and acquisition of a CRM are then observed (e.g., Oliva-Urcia et al., 2011; Oliva-Urcia & Kontny, 2012; Wang et al., 2020; Wang et al., 2021). For subaerial rocks in oxidizing conditions, growth of authigenic hematite and associated acquisition of CRM due to low-temperature hydrothermal alteration is widely reported in igneous and sedimentary units (e.g., Edel & Aifa, 2001; Geissman & Harlan, 2002; Huang et al., 2020). It has also been found that fine-grained authigenic maghemite formed during low-temperature fluid migration contributes to the acquisition of a CRM unblocking <600°C in Triassic terrestrial sandstones (Liu et al., 2011). An example of remagnetization caused by circulation of high-temperature hydrothermal fluids (>300°C) along local shear zones comes from Paleocene subaerial volcanic rocks from the Kohistan island arc in the western Himalayas. These rocks heterogeneously experienced two phases of greenschist and amphibolite facies metamorphism in two distinct time intervals, during which authigenic maghemite, magnetite, and hematite were formed and secondary NRMs were acquired (Ahmad et al., 2000).

In the E_1d lavas of the Linzizong Group that suffered from high-temperature hydrothermal alteration, we identified in our previous study that hematite—an authigenic magnetic mineral with broad size distribution and wide unblocking temperature spectrum—could induce remagnetization by acquiring CRMs in strongly to completely altered rocks (Huang, Dupont-Nivet, et al., 2015). Here, we further recognize that maghemite contributes to the acquisition of CRMs in the slightly to intermediately altered E_1d lavas. The inversion and unblocking temperature spectra of maghemite overlap with the unblocking temperature of the original Ti-poor titanomagnetite, leading to contamination and/or replacement of the primary remanence. Moreover, high-temperature hydrothermal alteration significantly reduced the grain size of the original MD titanomagnetite, rising the unblocking temperature range of the TVRM acquired during the hydrothermal events and leading to its unblocking in the same temperature range as the primary remanence. This observation explains the acquisition of normal polarity ITCs in a few type III samples: these ITCs reside in PSD-SD titanomagnetite and have a direction similar to the TVRM2 (Figures 2i; 5j; 7h).

Maghemitization, hematization, and grain size reduction of the primary (titano)magnetite during high-temperature hydrothermal alteration or metamorphic conditions, jeopardize the preservation of the primary remanence preservation. Future paleomagnetic investigations should consider these possibilities, particularly in rocks from orogenic settings where thermal anomalies and fluid circulation are common. The accompanying significant reduction of NRM intensity by maghemitization and hematization can be significant (Figure 2). High-temperature hydrothermal alteration thus provides a potential interpretation of the negative magnetic anomalies in continental igneous rock belts.

5. Conclusions

The Linzizong group in the Linzhou basin is the focus of paleomagnetic investigation of the Paleogene latitude of the Lhasa terrane before and during the India-Asia collision. The isolated ChRMs (ITC and HTC) from lavas of the lower Linzizong group (E_1d), which erupted at the key time interval of 69–58 Ma, have an abnormally

low inclination. These ChRMs, if primary, would indicate that the Lhasa terrane had experienced unrealistically fast northward and southward "yo-yo" motion during latest Cretaceous to Paleocene time and that the India-Asia collision had occurred in the equatorial humid belt. Here we reanalyze the thermal demagnetization data of these rocks and apply comprehensive rock magnetic and petrographic investigations, leading to the following conclusions.

1. The original magnetic carrier in the E_1d lavas is multi-domain Ti-poor titanomagnetite.
2. Titanomagnetite experienced significant grain size reduction and was variably converted to authigenic single-domain maghemite and hematite through redox and non-redox reactions in association with post-emplacement hydrothermal fluid flow.
3. The unblocking/inversion temperature spectra of maghemite and hematite overlap with those of titanomagnetite. The isolated intermediate and high temperature components from slightly to strongly altered E_1d lavas are a combination of primary remanence and a thermoviscous remanence carried by titanomagnetite, and CRM residing in maghemite and hematite. The primary remanence in completely altered E_1d lavas has been replaced by the chemical remanence residing in hematite and minor maghemite.
4. The low inclination of the isolated ChRMs isolated in the slightly altered lavas, and the directional consistence of intermediate and high temperature components in strongly to completely altered lavas, are due to the contamination and/or replacement of the primary remanence by thermoviscous remanence and chemical remanence in all of the E_1d lavas.
5. Hydrothermal alteration can jeopardize the primary remanence residing in titanomagnetite; such a remagnetization process involving maghemitization, hematization, and grain size reduction of titanomagnetite leads to destruction of the primary remanence and acquisition of thermoviscous and chemical remanence. Future paleomagnetic studies on rock units from orogenic belts with active thermal anomalies and fluid activities should carefully evaluate remagnetization induced by hydrothermal events.

Data Availability Statement

Rock magnetic data and EDS analysis results to support this article are available in Supporting Information S1 (Tables S1–S5 in Supporting Information S1). This data set is also deposited on Zenodo (https://doi.org/10.5281/zenodo.7691846).

Acknowledgments
We thank Dr. Thomas Berndt for the enlightening discussion on this work. Insightful and constructive comments from three reviewers, associate editors Dr. Adrian Muxworthy and Dr. Agnes Kontny, and editor Dr. Isabelle Manighetti have greatly helped to improve the original manuscript. This work was supported by the Second Tibetan Plateau Scientific Expedition and Research Program (STEP, Grant 2019QZKK0708) and the Natural Science Foundation of China (NSFC) project Basic Science Center for Tibetan Plateau Earth System (BCTES, Grant 41988101). W.H. was also supported by three visiting research fellowships from the Institute for Rock Magnetism (IRM) at the University of Minnesota, the IRM is a National multi-user facility funded by the NSF Instruments and Facilities program. This is IRM publication #2202.

References

Achache, J., Courtillot, V., & Xiu, Z. Y. (1984). Paleogeographic and tectonic evolution of southern Tibet since middle Cretaceous time: New paleomagnetic data and synthesis. *Journal of Geophysical Research: Solid Earth*, *89*(B12), 10311–10339. https://doi.org/10.1029/jb089ib12p10311

Ahmad, M. N., Yoshida, M., & Fujiwara, Y. (2000). Paleomagnetic study of Utror volcanic formation: Remagnetizations and postfolding rotations in Utror area, Kohistan arc, northern Pakistan. *Earth Planets and Space*, *52*(6), 425–436. https://doi.org/10.1186/bf03352254

Almeida, T. P., Kasama, T., Muxworthy, A. R., Williams, W., Nagy, L., Hansen, T. W., et al. (2014). Visualized effect of oxidation on magnetic recording fidelity in pseudo-single-domain magnetite particles. *Nature Communications*, *5*(1), 1–6. https://doi.org/10.1038/ncomms6154

Almeida, T. P., Muxworthy, A. R., Kasama, T., Williams, W., Damsgaard, C., Frandsen, C., et al. (2015). Effect of maghemization on the magnetic properties of nonstoichiometric pseudo-single-domain magnetite particles. *Geochemistry, Geophysics, Geosystems*, *16*(9), 2969–2979. https://doi.org/10.1002/2015gc005858

An, W., Hu, X., Garzanti, E., Wang, J. G., & Liu, Q. (2021). New precise dating of the India-Asia collision in the Tibetan Himalaya at 61 Ma. *Geophysical Research Letters*, *48*(3), e2020GL090641. https://doi.org/10.1029/2020gl090641

Appel, E. (1987). Stress anisotropy in Ti-rich titanomagnetites. *Physics of the Earth and Planetary Interiors*, *46*(1–3), 233–240. https://doi.org/10.1016/0031-9201(87)90185-3

Askill, J. (1970). *Tracer diffusion data for metals, alloys, and simple oxides*. IFI/Plcnum Data Corporation.

Berndt, T. A., & Chang, L. (2019). Theory of stable multi-domain thermoviscous remanence based on repeated domain-wall jumps. *Journal of Geophysical Research: Solid Earth*, *123*, 10399–10417. https://doi.org/10.11029/12018JB016816

Bian, W., Yang, T., Jiang, Z., Jin, J., Gao, F., Wang, S., et al. (2020). Paleomagnetism of the Late Cretaceous red beds from the far Western Lhasa terrane: Inclination discrepancy and tectonic implications. *Tectonics*, *39*(8), e2020TC006280. https://doi.org/10.1029/2020tc006280

Bilardello, D. (2020). Practical magnetism II: Humps and a bump, the maghemite song. *IRM Quarterly*, *30*(1), 1–16.

Bleil, U., & Petersen, N. (1983). Variations in magnetization intensity and low-temperature titanomagnetite oxidation of ocean floor basalts. *Nature*, *301*(5899), 384–388. https://doi.org/10.1038/301384a0

Bureau of Geology and Mineral Resources of Xizang (Tibet) Autonomous Region (BGMRXAR). (1993). *Regional geology of Xizang (Tibet) autonomous region, geological memoirs series* (Vol. 1, p. 707). Geological Publishing House. Number 31.

Butler, R. F. (1992). *Paleomagnetism: Magnetic domains to geologic terranes*. Blackwell Scientific Publications.

Cai, F., Ding, L., & Yue, Y. (2011). Provenance analysis of upper Cretaceous strata in the Tethys Himalaya, southern Tibet: Implications for timing of India-Asia collision. *Earth and Planetary Science Letters*, *305*(1–2), 195–206. https://doi.org/10.1016/j.epsl.2011.02.055

Chen, B., Ding, L., Xu, Q., Yue, Y., & Xie, J. (2016). U–Pb age framework of the Linzizong volcanic rocks from the Linzhou Basin, Tibet. *Quaternary Sciences*, *36*(5), 1037–1054.

Chen, J., Huang, B., & Sun, L. (2010). New constraints to the onset of the India-Asia collision: Paleomagnetic reconnaissance on the linzizong group in the Lhasa block, China. *Tectonophysics*, *489*(1–4), 189–209. https://doi.org/10.1016/j.tecto.2010.04.024

Chen, J., Huang, B., Yi, Z., Yang, L., & Chen, L. (2014). Paleomagnetic and $^{40}Ar/^{39}Ar$ geochronological results from the linzizong group, Linzhou basin, Lhasa terrane, Tibet: Implications to paleogene paleolatitude and onset of the India-Asia collision. *Journal of Asian Earth Sciences*, *96*, 162–177. https://doi.org/10.1016/j.jseaes.2014.09.007

Cui, Y., Verosub, K. L., & Roberts, A. P. (1994). The effect of low-temperature oxidation on large multi-domain magnetite. *Geophysical Research Letters*, *21*(9), 757–760. https://doi.org/10.1029/94gl00639

Da Costa, G., De Grave, E., Bowen, L., De Bakker, P., & Vandenberghe, R. (1995). Temperature dependence of the hyperfine parameters of maghemite and Al-substituted maghemites. *Physics and Chemistry of Minerals*, *22*(3), 178–185. https://doi.org/10.1007/bf00202298

Davis, B. L., Rapp, G., & Walawender, M. J. (1968). Fabric and structural characteristics of the martitization process. *American Journal of Science*, *266*(6), 482–496. https://doi.org/10.2475/ajs.266.6.482. https://www.ajsonline.org/content/ajs/266/6/482.full.pdf

De Boer, C. B., Mullender, T. A., & Dekkers, M. J. (2001). Low-temperature behaviour of haematite: Susceptibility and magnetization increase on cycling through the Morin transition. *Geophysical Journal International*, *146*(1), 201–216. https://doi.org/10.1046/j.0956-540x.2001.01443.x

DeCelles, P., Kapp, P., Gehrels, G., & Ding, L. (2014). Paleocene-Eocene foreland basin evolution in the Himalaya of southern Tibet and Nepal: Implications for the age of initial India-Asia collision. *Tectonics*, *33*(5), 824–849. https://doi.org/10.1002/2014TC003522

Ding, L., Kapp, P., Zhong, D., & Deng, W. (2003). Cenozoic volcanism in Tibet: Evidence for a transition from oceanic to continental subduction. *Journal of Petrology*, *44*(10), 1833–1865. https://doi.org/10.1093/petrology/egg061

Ding, L., Qasim, M., Jadoon, I. A., Khan, M. A., Xu, Q., Cai, F., et al. (2016). The India–Asia collision in north Pakistan: Insight from the U–Pb detrital zircon provenance of Cenozoic foreland basin. *Earth and Planetary Science Letters*, *455*, 49–61. https://doi.org/10.1016/j.epsl.2016.09.003

Ding, L., Xu, Q., Yue, Y., Wang, H., Cai, F., & Li, S. (2014). The Andean-type Gangdese Mountains: Paleoelevation record from the Paleocene–eocene Linzhou basin. *Earth and Planetary Science Letters*, *392*, 250–264. https://doi.org/10.1016/j.epsl.2014.01.045

Doriguetto, A., Fernandes, N., Persiano, A., Nunes Filho, E., Greneche, J., & Fabris, J. (2003). Characterization of a natural magnetite. *Physics and Chemistry of Minerals*, *30*(5), 249–255. https://doi.org/10.1007/s00269-003-0310-x

Doubrovine, P. V., & Tarduno, J. A. (2004). Self-reversed magnetization carried by titanomaghemite in oceanic basalts. *Earth and Planetary Science Letters*, *222*(3), 959–969. https://doi.org/10.1016/j.epsl.2004.04.009

Doubrovine, P. V., & Tarduno, J. A. (2006). Alteration and self-reversal in oceanic basalts. *Journal of Geophysical Research*, *111*(B12). https://doi.org/10.1029/2006jb004468

Dunlop, D. J. (2002). Theory and application of the day plot (M_{rs}/M_s versus H_{cr}/H_c) 2. Application to data for rocks, sediments, and soils. *Journal of Geophysical Research*, *107*(B3), 2057. https://doi.org/10.1029/2001JB000487

Dunlop, D. J., & Ödemir, Ö. (1997). *Rock magnetism: Fundamentals and frontiers*. Cambridge University Press.

Dupont-Nivet, G., Lippert, P. C., Van Hinsbergen, D. J. J., Meijers, M. J. M., & Kapp, P. (2010). Palaeolatitude and age of the Indo-Asia collision: Palaeomagnetic constraints. *Geophysical Journal International*, *182*(3), 1189–1198. https://doi.org/10.1111/j.1365-246x.2010.04697.x

Dyar, M. D., Agresti, D. G., Schaefer, M. W., Grant, C. A., & Sklute, E. C. (2006). Mössbauer spectroscopy of Earth and planetary materials. *Annual Review of Earth and Planetary Sciences*, *34*(1), 83–125. https://doi.org/10.1146/annurev.earth.34.031405.125049

Edel, J. B., & Aifa, T. (2001). Paleomagnetic evolution of the Armorican Massif in late Paleozoic times, in the light of overprints recorded in Cadomian and Paleozoic units. *Tectonophysics*, *331*(1), 145–167. https://doi.org/10.1016/s0040-1951(00)00240-7

Elmore, R. D., Muxworthy, A. R., & Aldana, M. (2012). Remagnetization and chemical alteration of sedimentary rocks. *Geological Society, London, Special Publications*, *371*(1), 1–21. https://doi.org/10.1144/sp371.15

Fabian, K. (2009). Thermochemical remanence acquisition in single-domain particle ensembles: A case for possible overestimation of the geomagnetic paleointensity. *Geochemistry, Geophysics, Geosystems*, *10*(6). https://doi.org/10.1029/2009gc002420

Fabian, K., & Shcherbakov, V. P. (2020). The magnetization of the ocean floor: Stress and fracturing of titanomagnetite particles by low-temperature oxidation. *Geophysical Journal International*, *221*(3), 2104–2112. https://doi.org/10.1093/gji/ggaa142

Font, E., Rapalini, A., Tomezzoli, R., Trindade, R., & Tohver, E. (2012). Episodic remagnetizations related to tectonic events and their consequences for the South America polar wander path. *Geological Society, London, Special Publications*, *371*(1), 55–87. https://doi.org/10.1144/sp371.7

Ge, K., Williams, W., Liu, Q., & Yu, Y. (2014). Effects of the core-shell structure on the magnetic properties of partially oxidized magnetite grains: Experimental and micromagnetic investigations. *Geochemistry, Geophysics, Geosystems*, *15*(5), 2021–2038. https://doi.org/10.1002/2014GC005265

Gehring, A. U., Fischer, H., Louvel, M., Kunze, K., & Weidler, P. G. (2009). High temperature stability of natural maghemite: A magnetic and spectroscopic study. *Geophysical Journal International*, *179*(3), 1361–1371. https://doi.org/10.1111/j.1365-246X.2009.04348.x

Geissman, J. W., & Harlan, S. S. (2002). Late Paleozoic remagnetization of Precambrian crystalline rocks along the Precambrian/Carboniferous nonconformity, rocky mountains: A relationship among deformation, remagnetization, and fluid migration. *Earth and Planetary Science Letters*, *203*(3), 905–924. https://doi.org/10.1016/s0012-821x(02)00932-9

Gendler, T., Shcherbakov, V., Dekkers, M., Gapeev, A., Gribov, S., & McClelland, E. (2005). The lepidocrocite–maghemite–haematite reaction chain—I. Acquisition of chemical remanent magnetization by maghemite, its magnetic properties and thermal stability. *Geophysical Journal International*, *160*(3), 815–832. https://doi.org/10.1111/j.1365-246x.2005.02550.x

Gribov, S., Dolotov, A., & Shcherbakov, V. (2017). Experimental modeling of the chemical remanent magnetization and Thellier procedure on titanomagnetite-bearing basalts. *Izvestiya - Physics of the Solid Earth*, *53*(2), 274–292. https://doi.org/10.1134/s1069351317010062

Guyodo, Y., Mostrom, A., Penn, R. L., & Banerjee, S. K. (2003). From nanodots to nanorods: Oriented aggregation and magnetic evolution of nanocrystalline goethite. *Geophysical Research Letters*, *30*(10), a–n. https://doi.org/10.1029/2003GL017021

Harrison, R. J., & Feinberg, J. M. (2008). FORCinel: An improved algorithm for calculating first-order reversal curve distributions using locally weighted regression smoothing. *Geochemistry, Geophysics, Geosystems*, *9*(5), Q05016. https://doi.org/10.1029/2008gc001987

Harrison, R. J., Zhao, X., Hu, P., Sato, T., Heslop, D., Muxworthy, A. R., et al. (2019). Simulation of remanent, transient, and induced FORC diagrams for interacting particles with uniaxial, cubic, and hexagonal anisotropy. *Journal of Geophysical Research: Solid Earth*, *124*(12), 12404–12429. https://doi.org/10.1029/2019jb018050

He, S., Kapp, P., DeCelles, P. G., Gehrels, G. E., & Heizler, M. (2007). Cretaceous-tertiary geology of the Gangdese arc in the Linzhou area, southern Tibet. *Tectonophysics*, *433*(1–4), 15–37. https://doi.org/10.1016/j.tecto.2007.01.005

Housden, J., & O'Reilly, W. (1990). On the intensity and stability of the natural remanent magnetization of ocean floor basalts. *Physics of the Earth and Planetary Interiors*, *64*(2–4), 261–278. https://doi.org/10.1016/0031-9201(90)90042-v

Hu, X., Garzanti, E., Moore, T., & Raffi, I. (2015). Direct stratigraphic dating of India-Asia collision onset at the Selandian (middle Paleocene, 59±1 Ma). *Geology*, *43*(10), 859–862. https://doi.org/10.1130/g36872.1

Hu, X., Garzanti, E., Wang, J., Huang, W., An, W., & Webb, A. (2016). The timing of India-Asia collision onset–facts, theories, controversies. *Earth-Science Reviews*, *160*, 264–299. https://doi.org/10.1016/j.earscirev.2016.07.014

Huang, W., Dupont-Nivet, G., Lippert, P. C., Van Hinsbergen, D. J. J., Dekkers, M. J., Guo, Z., et al. (2015). Can a primary remanence be retrieved from partially remagnetized Eocence volcanic rocks in the Nanmulin Basin (southern Tibet) to date the India-Asia collision? *Journal of Geophysical Research: Solid Earth*, *120*(1), 42–66. https://doi.org/10.1002/2014jb011599

Huang, W., Dupont-Nivet, G., Lippert, P. C., Van Hinsbergen, D. J. J., Dekkers, M. J., Waldrip, R., et al. (2015). What was the paleogene latitude of the Lhasa terrane? A reassessment of the geochronology and paleomagnetism of linzizong volcanic rocks (Linzhou basin, Tibet). *Tectonics*, *34*(3), 594–622. https://doi.org/10.1002/2014tc003787

Huang, W., Dupont-Nivet, G., Lippert, P. C., Van Hinsbergen, D. J. J., & Hallot, E. (2013). Inclination shallowing in eocene linzizong sedimentary rocks from southern Tibet: Correction, possible causes and implications for reconstructing the India–Asia collision. *Geophysical Journal International*, *194*(3), 1390–1411. https://doi.org/10.1093/gji/ggt188

Huang, W., Jackson, M. J., Dekkers, M. J., Solheid, P., Zhang, Y., Li, S., et al. (2020). Remagnetization of red beds on the Tibetan plateau: Mechanism and diagnosis. *Journal of Geophysical Research: Solid Earth*, *125*(8), e2020JB020068. https://doi.org/10.1029/2020jb020068

Huang, W., Lippert, P. C., Reiners, P. W., Quade, J., Kapp, P., Ganerod, M., et al. (2022). Hydrothermal events in the Linzizong group: Implications for Paleogene exhumation and paleoaltimetry of the southern Tibetan Plateau. *Earth and Planetary Science Letters*, *583*, 117390. https://doi.org/10.1016/j.epsl.2022.117390

Huang, W., Lippert, P. C., Reiners, P. W., Quade, J., Kapp, P., Ganerød, M., et al. (2023). Reply to comment by Zhao et al. on "hydrothermal events in the Linzizong group: Implications for Paleogene exhumation and paleoaltimetry of the southern Tibetan Plateau". *Earth and Planetary Science Letters*, *603*, 117973. https://doi.org/10.1016/j.epsl.2022.117973

Ingalls, M., Rowley, D., Olack, G., Currie, B., Li, S., Schmidt, J., et al. (2018). Paleocene to Pliocene low-latitude, high-elevation basins of southern Tibet: Implications for tectonic models of India-Asia collision, Cenozoic climate, and geochemical weathering. *GSA Bulletin*, *130*(1–2), 307–330. https://doi.org/10.1130/b31723.1

Jackson, M. J., & Moskowitz, B. (2021). On the distribution of Verwey transition temperatures in natural magnetites. *Geophysical Journal International*, *224*(2), 1314–1325. https://doi.org/10.1093/gji/ggaa516

Jolivet, J.-P., & Tronc, E. (1988). Interfacial electron transfer in colloidal spinel iron oxide. Conversion of Fe3O4-γFe2O3 in aqueous medium. *Journal of Colloid and Interface Science*, *125*(2), 688–701. https://doi.org/10.1016/0021-9797(88)90036-7

Kontny, A., & Grothaus, L. (2017). Effects of shock pressure and temperature on titanomagnetite from ICDP cores and target rocks of the El'gygytgyn impact structure, Russia. *Studia Geophysica et Geodaetica*, *61*(1), 162–183. https://doi.org/10.1007/s11200-016-0819-3

Kontny, A., Vahle, C., & De Wall, H. (2003). Characteristic magnetic behavior of subaerial and submarine lava units from the Hawaiian Scientific Drilling Project (HSDP-2). *Geochemistry, Geophysics, Geosystems*, *4*(2). https://doi.org/10.1029/2002gc000304

Kosterov, A. (2002). Low-temperature magnetic hysteresis properties of partially oxidized magnetite. *Geophysical Journal International*, *149*(3), 796–804. https://doi.org/10.1046/j.1365-246x.2002.01686.x

Kosterov, A., & Fabian, K. (2008). Twinning control of magnetic properties of multidomain magnetite below the Verwey transition revealed by measurements on individual particles. *Geophysical Journal International*, *174*(1), 93–106. https://doi.org/10.1111/j.1365-246x.2008.03811.x

Koymans, M. R., Hinsbergen, D., Pastor-Galán, D., Vaes, B., & Langereis, C. G. (2020). Towards FAIR paleomagnetic data management through Paleomagnetism.org 2.0. *Geochemistry, Geophysics, Geosystems*, *21*(2), e2019GC008838. https://doi.org/10.1029/2019gc008838

Koymans, M. R., Langereis, C. G., Pastor-Galán, D., & Van Hinsbergen, D. J. (2016). Paleomagnetism. Org: An online multi-platform open source environment for paleomagnetic data analysis. *Computers & Geosciences*, *93*, 127–137. https://doi.org/10.1016/j.cageo.2016.05.007

Krása, D., Shcherbakov, V. P., Kunzmann, T., & Petersen, N. (2005). Self-reversal of remanent magnetization in basalts due to partially oxidized titanomagnetites. *Geophysical Journal International*, *162*(1), 115–136. https://doi.org/10.1111/j.1365-246x.2005.02656.x

Lattard, D., Engelmann, R., Kontny, A., & Sauerzapf, U. (2006). Curie temperatures of synthetic titanomagnetites in the Fe-Ti-O system: Effects of composition, crystal chemistry, and thermomagnetic methods. *Journal of Geophysical Research*, *111*(B12). https://doi.org/10.1029/2006jb004591

Lipka, J., Madsen, M., Orlicky, D., Koch, C., & Mørup, S. (1988). A study of titanomagnetites in basaltic rocks from Nigeria. *Physica Scripta*, *38*(3), 508–512. https://doi.org/10.1088/0031-8949/38/3/033

Lippert, P. C., Van Hinsbergen, D. J. J., & Dupont-Nivet, G. (2014). The early cretaceous to present latitude of the central Lhasa-plano (Tibet): A paleomagnetic synthesis with implications for Cenozoic tectonics, paleogeography and climate of Asia. In J. S. Nie, G. D. Hoke, & B. K. Horton (Eds.), *Towards an improved understanding of uplift mechanisms and the elevation history of the Tibetan plateau, Geological Society of America Special Paper* (Vol. 507, pp. 1–21). Geological Society of America.

Liu, C., Ge, K., Zhang, C., Liu, Q., Deng, C., & Zhu, R. (2011). Nature of remagnetization of Lower Triassic red beds in southwestern China. *Geophysical Journal International*, *187*(3), 1237–1249. https://doi.org/10.1111/j.1365-246x.2011.05196.x

Liu, H. (1993). Classification and age attribution of the Linzizong volcanic series in the Lhasa area of Tibet. *Tibetan Geology*, *10*(2), 59–68. (in Chinese).

Liu, Q., Banerjee, S. K., Jackson, M. J., Deng, C., Pan, Y., & Rixiang, Z. (2004). New insights into partial oxidation model of magnetites and thermal alteration of magnetic mineralogy of the Chinese loess in air. *Geophysical Journal International*, *158*(2), 506–514. https://doi.org/10.1111/j.1365-246x.2004.02348.x

Ma, Y., Yang, T., Bian, W., Jin, J., Wang, Q., Zhang, S., et al. (2017). Paleomagnetic and geochronologic results of latest cretaceous lava flows from the Lhasa terrane and their tectonic implications. *Journal of Geophysical Research: Solid Earth*, *122*(11), 8786–8809. https://doi.org/10.1002/2017JB014743

Matzka, J., Krása, D., Kunzmann, T., Schult, A., & Petersen, N. (2003). Magnetic state of 10–40 Ma old ocean basalts and its implications for natural remanent magnetization. *Earth and Planetary Science Letters*, *206*(3–4), 541–553. https://doi.org/10.1016/s0012-821x(02)01094-4

Maxbauer, D. P., Feinberg, J. M., & Fox, D. L. (2016). Max UnMix: A web application for unmixing magnetic coercivity distributions. *Computers & Geosciences*, *95*, 140–145. https://doi.org/10.1016/j.cageo.2016.07.009

Mo, X., Zhao, Z., Deng, J., Dong, G. C., Zhou, S., Guo, T. Y., et al. (2003). Response of volcanism to the India-Asia collision. *Earth Science Frontiers*, *10*(3), 135–148.

Murad, E., & Cashion, J. (2004). Iron oxides. In *Mössbauer spectroscopy of environmental materials and their industrial utilization* (pp. 159–188). Springer. https://doi.org/10.1007/978-1-4419-9040-2_5

Muxworthy, A. R., King, J. G., & Heslop, D. (2005). Assessing the ability of first-order reversal curve (FORC) diagrams to unravel complex magnetic signals. *Journal of Geophysical Research*, *110*(B1), B01105. https://doi.org/10.1029/2004jb003195

Ohmoto, H. (2003). Nonredox transformations of magnetite-hematite in hydrothermal systems. *Economic Geology*, *98*(1), 157–161. https://doi.org/10.2113/gsecongeo.98.1.157

Oliva-Urcia, B., & Kontny, A. (2012). Remanent magnetization of maghemitized basalts from Krafla drill cores, NE-Iceland. *Studia Geophysica et Geodaetica*, *56*(3), 641–657. https://doi.org/10.1007/s11200-011-9013-9

Oliva-Urcia, B., Kontny, A., Vahle, C., & Schleicher, A. M. (2011). Modification of the magnetic mineralogy in basalts due to fluid–rock interactions in a high-temperature geothermal system (Krafla, Iceland). *Geophysical Journal International*, *186*(1), 155–174. https://doi.org/10.1111/j.1365-246x.2011.05029.x

Otake, T., Wesolowski, D. J., Anovitz, L. M., Allard, L. F., & Ohmoto, H. (2007). Experimental evidence for non-redox transformations between magnetite and hematite under H_2-rich hydrothermal conditions. *Earth and Planetary Science Letters*, *257*(1–2), 60–70. https://doi.org/10.1016/j.epsl.2007.02.022

Özdemir, Ö., & Dunlop, D. J. (1985). An experimental study of chemical remanent magnetizations of synthetic monodomain titanomaghemites with initial thermoremanent magnetizations. *Journal of Geophysical Research*, *90*(B13), 11513–11523. https://doi.org/10.1029/jb090ib13p11513

Özdemir, Ö., & Dunlop, D. J. (2010). Hallmarks of maghemitization in low-temperature remanence cycling of partially oxidized magnetite nanoparticles. *Journal of Geophysical Research*, *115*(B2), B02101. https://doi.org/10.01029/02009JB006756

Roberts, A. P., Heslop, D., Zhao, X., & Pike, C. R. (2014). Understanding fine magnetic particle systems through use of first-order reversal curve diagrams. *Reviews of Geophysics*, *52*(4), 557–602. https://doi.org/10.1002/2014rg000462

Roberts, A. P., Tauxe, L., Heslop, D., Zhao, X., & Jiang, Z. (2018). A critical appraisal of the 'Day' diagram. *Journal of Geophysical Research: Solid Earth*, *123*(4), 2618–2644. https://doi.org/10.1002/2017JB015247

Roberts, A. P., Zhao, X., Hu, P., Abrajevitch, A., Chen, Y. H., Harrison, R. J., et al. (2021). Magnetic domain state and anisotropy in hematite (α-Fe_2O_3) from first-order reversal curve diagrams. *Journal of Geophysical Research: Solid Earth*, *126*(12), e2021JB023027. https://doi.org/10.1029/2021jb023027

Swanson-Hysell, N. L., Fairchild, L. M., & Slotznick, S. P. (2019). Primary and secondary red bed magnetization constrained by fluvial intraclasts. *Journal of Geophysical Research: Solid Earth*, *124*(5), 4276–4289. https://doi.org/10.1029/2018jb017067

Swanson-Hysell, N. L., Feinberg, J. M., Berquó, T. S., & Maloof, A. C. (2011). Self-reversed magnetization held by martite in basalt flows from the 1.1-billion-year-old Keweenawan rift, Canada. *Earth and Planetary Science Letters*, *305*(1–2), 171–184. https://doi.org/10.1016/j.epsl.2011.02.053

Tan, X., Gilder, S., Kodama, K. P., Jiang, W., Han, Y., Zhang, H., et al. (2010). New paleomagnetic results from the Lhasa block: Revised estimation of latitudinal shortening across Tibet and implications for dating the India-Asia collision. *Earth and Planetary Science Letters*, *293*(3), 396–404. https://doi.org/10.1016/j.epsl.2010.03.013

Tang, J., Myers, M., Bosnick, K. A., & Brus, L. E. (2003). Magnetite Fe_3O_4 nanocrystals: Spectroscopic observation of aqueous oxidation kinetics. *The Journal of Physical Chemistry B*, *107*(30), 7501–7506. https://doi.org/10.1021/jp027048e

Tauxe, L., Bertram, H. N., & Seberino, C. (2002). Physical interpretation of hysteresis loops: Micromagnetic modeling of fine particle magnetite. *Geochemistry, Geophysics, Geosystems*, *3*(10), 1–22. https://doi.org/10.1029/2001gc000241

Tauxe, L., Mullender, T., & Pick, T. (1996). Potbellies, wasp-waists, and superparamagnetism in magnetic hysteresis. *Journal of Geophysical Research*, *101*(B1), 571–583. https://doi.org/10.1029/95jb03041

Thomas, N. (1993). An integrated rock magnetic approach to the selection or rejection of ancient basalt samples for palaeointensity experiments. *Physics of the Earth and Planetary Interiors*, *75*(4), 329–342. https://doi.org/10.1016/0031-9201(93)90008-w

Van Velzen, A., & Zijderveld, J. (1995). Effects of weathering on single-domain magnetite in early Pliocene marine marls. *Geophysical Journal International*, *121*(1), 267–278. https://doi.org/10.1111/j.1365-246x.1995.tb03526.x

Verwey, E. (1939). Electronic conduction of magnetite (Fe_3O_4) and its transition point at low temperatures. *Nature*, *144*(3642), 327–328. https://doi.org/10.1038/144327b0

Wang, D., & Van der Voo, R. (2004). The hysteresis properties of multidomain magnetite and titanomagnetite/titanomaghemite in mid-ocean ridge basalts. *Earth and Planetary Science Letters*, *220*(1), 175–184. https://doi.org/10.1016/s0012-821x(04)00052-4

Wang, S., Chang, L., Tao, C., Bilardello, D., Liu, L., & Wu, T. (2021). Seafloor magnetism under hydrothermal alteration: Insights from magnetomineralogy and magnetic properties of the southwest Indian ridge basalts. *Journal of Geophysical Research: Solid Earth*, *126*(12), e2021JB022646. https://doi.org/10.1029/2021jb022646

Wang, S., Chang, L., Wu, T., & Tao, C. (2020). Progressive dissolution of titanomagnetite in high-temperature hydrothermal vents dramatically reduces magnetization of Basaltic ocean crust. *Geophysical Research Letters*, *47*(8), e2020GL087578. https://doi.org/10.1029/2020gl087578

Xing, Y., Brugger, J., Etschmann, B., Tomkins, A. G., Frierdich, A. J., & Fang, X. (2021). Trace element catalyses mineral replacement reactions and facilitates ore formation. *Nature Communications*, *12*(1), 1–7. https://doi.org/10.1038/s41467-021-21684-5

Xu, W., Van der Voo, R., Peacor, D. R., & Beaubouef, R. T. (1997). Alteration and dissolution of fine-grained magnetite and its effects on magnetization of the ocean floor. *Earth and Planetary Science Letters*, *151*(3–4), 279–288. https://doi.org/10.1016/s0012-821x(97)81854-7

Yapp, C. J. (1990). Oxygen isotopes in iron (III) oxides: 1. Mineral-Water fractionation factors. *Chemical Geology*, *85*(3–4), 329–335. https://doi.org/10.1016/0009-2541(90)90010-5

Yi, Z., Wang, T., Meert, J. G., Zhao, Q., & Liu, Y. (2021). An initial collision of India and Asia in the equatorial humid belt. *Geophysical Research Letters*, *48*(9), e2021GL093408. https://doi.org/10.1029/2021gl093408

Yin, A., & Harrison, M. T. (2000). Geologic evolution of the Himalayan-Tibetan orogen. *Annual Review of Earth and Planetary Sciences*, *28*(1), 211–280. https://doi.org/10.1146/annurev.earth.28.1.211

Yin, S., Wirth, R., He, H., Ma, C., Pan, J., Xing, J., et al. (2022). Replacement of magnetite by hematite in hydrothermal systems: A refined redox-independent model. *Earth and Planetary Science Letters*, *577*, 117282. https://doi.org/10.1016/j.epsl.2021.117282

Yue, Y., & Ding, L. (2006). $^{40}Ar/^{39}Ar$ geochronology, geochemical characteristics and Genesis of the Linzhou basic dikes, Tibet. *Acta Petrologica Sinica*, *22*(4), 855–866.

Zhang, Q., Appel, E., Basavaiah, N., Hu, S., Zhu, X., & Neumann, U. (2021). Is alteration of magnetite during rock weathering climate-dependent? *Journal of Geophysical Research: Solid Earth*, *126*(10), e2021JB022693. https://doi.org/10.1029/2021jb022693

Zhao, J., Brugger, J., & Pring, A. (2019). Mechanism and kinetics of hydrothermal replacement of magnetite by hematite. *Geoscience Frontiers*, *10*(1), 29–41. https://doi.org/10.1016/j.gsf.2018.05.015